CHALMERS
UNIVERSITY OF TECHNOLOGY

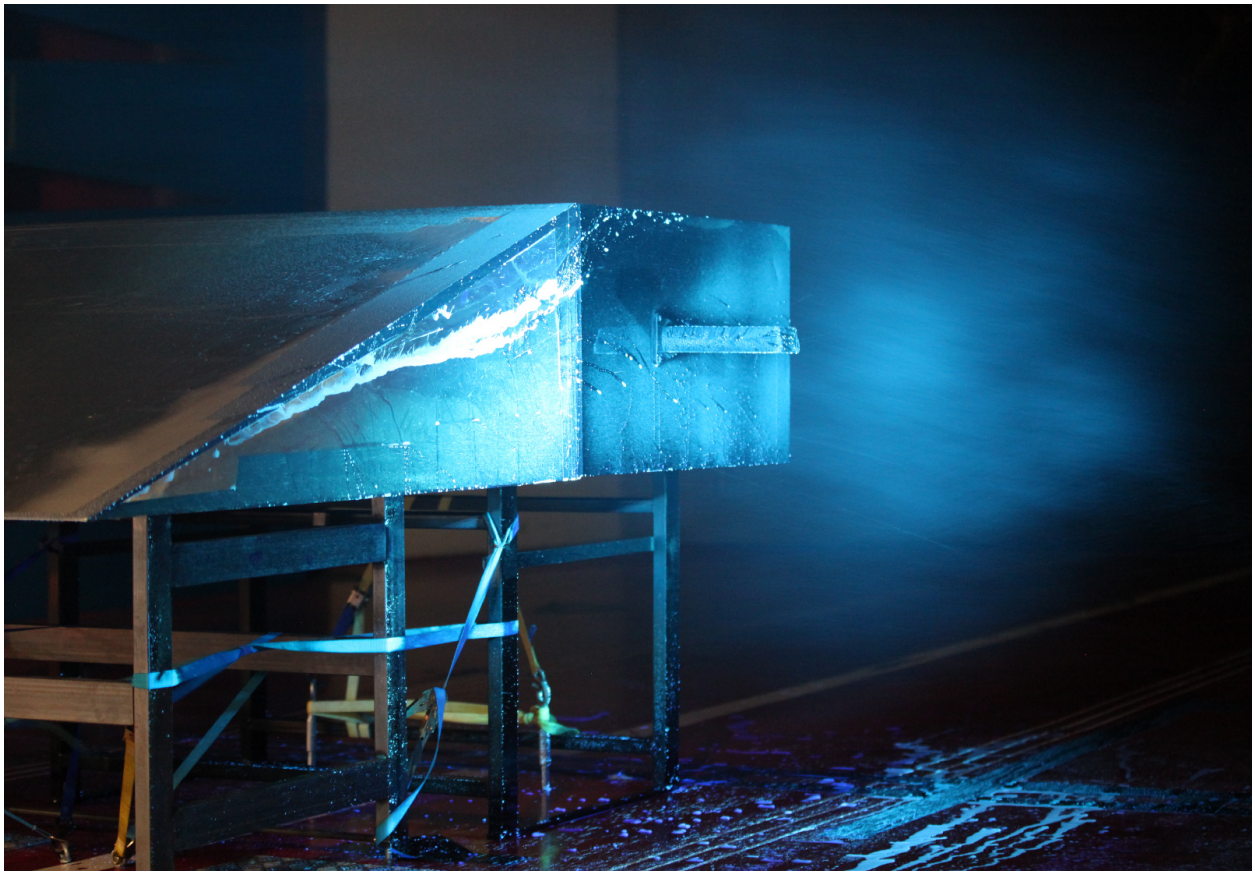

Water Contamination of a Side View Camera Monitoring System

Understanding how driving conditions and design features affect dynamics of airborne droplets using CFD and experiments

Master thesis in Innovative and Sustainable Chemical Engineering

Oskar Hamidi

Department of Mechanics and Maritime Sciences
CHALMERS UNIVERSITY OF TECHNOLOGY
Gothenburg, Sweden 2023

Master Thesis

Water Contamination of a Side View Camera Monitoring System

Understanding how driving conditions and design features affect dynamics of airborne droplets using CFD and experiments

Master thesis in Innovative and Sustainable Chemical Engineering

Oskar Hamidi

CHALMERS
UNIVERSITY OF TECHNOLOGY

Department of Mechanics and Maritime Sciences
Division of Fluid Dynamics
Chalmers University of Technology
Göteborg, Sweden 2023

Water Contamination of a Side View Camera Monitoring System
Understanding how driving conditions and design features affect dynamics of airborne droplets using CFD and experiments

Oskar Hamidi

Industrial Supervisor:
Tobias Eidevåg
Technical Expert, Contamination
Volvo Cars Corporation

Examiner:
Henrik Ström
Professor - Fluid Dynamics
Department of Mechanics and Maritime Sciences
Chalmers University of Technology

Master Thesis
Department of Mechanics and Maritime Sciences
Division of Fluid Dynamics
Chalmers University of Technology
SE-412 96 Göteborg
Telephone +46 31 772 1000

Cover: Test object in wind tunnel

Typeset in LaTeX
Printed by Department of Mechanics and Maritime Sciences
Gothenburg, Sweden 2023

Water Contamination of a Side View Camera Monitoring System
Understanding how driving conditions and design features affect dynamics of airborne droplets using CFD and experiments
Oskar Hamidi
Department of Mechanics and Maritime Sciences
Chalmers University of Technology

Abstract

Every year, an estimated 1.3 million lives are lost in traffic collisions. To make driving safer, hazard detecting safety technology is continuously developed, relying on sensors such as cameras to monitor the road. A side view Camera Monitoring System is a technology that enables wider rear view vision, revealing the driver's blind-spot and overall increases visibility in dusk and dawn glaring-conditions. However, the camera is susceptible to soiling by water droplets, obstructing its lens and hindering its function. This project aimed to increase the understanding of airborne water droplet contamination of a prototype Camera Monitoring System, designed specifically for the project. The theoretical droplet dynamics were used to derive a computational model capable of simulating the problem in Simcenter STAR-CCM+ using an Eulerian-Lagrangian approach on a simplified aerodynamic body in different driving conditions. Design features of the prototype were evaluated by altering the shape of its glareshield, adding a drainage groove and streamlining the flow at its arm. The designs and bluff body were all tested in Volvo Cars Aerodynamic Wind Tunnel to produce comparable results to the simulations. The project concluded that majority of airborne droplets within the camera's wake region deform, with some fragmenting into smaller droplets. Subsequently, the droplet drag force would be underestimated if deformation was excluded from the drag model. Drag was also the most significant droplet force, although both gravity and pressure gradient forces became significant for larger droplets, with the latter increasing their response to the flow. Few of the smallest droplets from the primary road spray would soil the prototype, instead airborne droplets would mostly originate from rupturing films of accumulated water at the face's circumference. Most of the larger droplets would not reach the lens, but deposition size would increase with driving velocity. Grounded droplets were observed migrating to the camera face instead of rupturing in experiments, where they could coalesce with other deposited droplets to form a self-cleaning mechanism, although the likelihood of favoring film ruptures would increase with driving velocity. The simulated ideal drainage groove only permitted the smallest droplets to soil the camera, whilst the real groove would overflow which would permit larger droplets to reach the face, but it did also prevent the migrations. A deeper or wider glareshield would reduce soiling, but when slanted the glareshield would be more susceptible to soiling in both experiments and simulations. Finally, the size of the camera's wake would decrease when flattening its arm, leading to a reduction in contamination.

Keywords: CFD, CMS, Contamination, Droplets, Film Rupture, Multiphase, Road Spray, Vehicle Aerodynamics, Wind Tunnel

Preface

This project was preformed at the department of Mechanics and Maritime Sciences at Chalmers University of Technology in cooperation with Volvo Cars Corporation. The project was started in January 2023 and mainly performed at Volvo Cars in Torslanda, Sweden. It was finally presented in June 2023 at Chalmers.

I would like to thank the engineers at Contamination for continuous support and advice. In particular, I would like to thank David Kallin for always challenging my understanding of the results. I would also like to thank the workshop technicians for constructing the Wedgeoid and the wind tunnel operatives for setting it up for experiments.

A special thanks to Martin Larsson who went out and beyond to make the CAD of the CMS prototypes used in this project. I thank you for ensuring that they were all 3D-printed on time and everything else you did to ensure to possibilities of this project.

I would also like to thank my examiner Henrik Ström for always being available to meet and discuss the project, and for providing a different perspective on problems.

Finally, I would like to direct a big thanks to the mind behind the project, my industrial supervisor Tobias Eidevåg, for always challenging my ambition and pushing me to reach further possibilities. I would also like to thank you for being so invested in the project and always finding solutions to the problems that would arise.

Contents

List of Figures

List of Tables

Nomenclature

Abbreviations

ADAS	Advanced Driver Assistance System
CFD	Computational Fluid Dynamics
CMS	Camera Monitoring System
DDES	Delayed-Detached Eddy Simulation
FVM	Finite Volume Method
GS	Glareshield
LES	Large Eddy Simulation
RANS	Reynolds Averaged Navier-Stokes
TAB	Taylor Analogy Breakup

Latin Symbols

B	Wall function parameter	$[-]$
C_B	TAB empirical constant	$[-]$
C_D	Drag force coefficient	$[-]$
$C_{D,sphere}$	Spherical drag force coefficient	$[-]$
C_{DES}	DES constant	$[-]$
C_L	Shear lift force coefficient	$[-]$
C_v	Eddy viscosity constant	$[-]$
CFL	Convective Courant number	$[-]$
D_s	Stable droplet diameter	$[m]$
d	Distance to boundary	$[m]$
d_{def}	Deformed particle diameter	$[m]$
d_p	Particle diameter	$[m]$
$\tilde{d}$	DDES length parameter	$[m]$
F_D	Drag force	$[N]$
$\mathcal{F}_d$	DDES function	$[-]$
F_G	Gravity force	$[N]$
F_P	Pressure gradient force	$[N]$
F_S	Shear lift force	$[N]$
F_{VM}	Virtual mass force	$[N]$
G	LES filter function	$[-]$
g	Gravitational constant	$[m/s^2]$
K	Von Kármán constant	$[-]$
k	Turbulent kinetic Energy	$[J]$
l	Turbulent length scale	$[m]$
l_0	Characteristic length	$[m]$
m_p	Particle mass	$[m]$
Oh	Ohnesorge number	$[-]$
P	Pressure	$[N/m^2]$
Re	Reynolds number	$[-]$
Re_p	Reynolds particle Number	$[-]$
Re_s	Reynolds shear Number	$[-]$
σ_p	Particle surface tension	$[kg/s^2]$
Stk	Stokes number	$[-]$
T	Time spent in eddy	$[s]$
t	Time	$[s]$
U_f	Fluid velocity	$[m/s]$
$U_{f,\Delta}$	Filtered fluid velocity	$[m/s]$
U_p	Particle velocity	$[m/s]$
U_s	Slip velocity	$[m/s]$
U^+	Dimensionless friction velocity	$[-]$
u'_f	Fluid fluctuation velocity	$[m/s]$
V	Volume	$[m^3]$
We	Weber number	$[-]$
x	Space	$[m]$

x_p	Particle position	$[m]$
x_{dis}	TAB displacement	$[m]$
x'	Sub-grid length scale	$[m]$
y	Distortion parameter	$[-]$
y^+	Dimensionless wall distance	$[-]$
y_{TAB}	TAB distortion parameter	$[-]$
y_w	Wall distance	$[m]$

Greek Symbols

β	Shear lift parameter	$[-]$
ϵ	Turbulent dissipation rate	$[J/s]$
Δ	Grid spacing	$[m]$
μ_f	Fluid dynamic viscosity	$[N \times s/m^2]$
μ_p	Particle dynamic viscosity	$[N \times s/m^2]$
ω_f	Fluid vorticity	$[/s]$
π	Mathematical constant	$[-]$
ρ_f	Fluid density	$[kg/m^3]$
ρ_p	Particle density	$[kg/m^3]$
τ_b	Reitz-Diwakar characteristic time	$[s]$
τ_f	Characteristic flow time	$[s]$
τ_p	Particle response time	$[s]$
τ_w	Wall shear stress	$[N/m^2]$
υ_f	Fluid kinematic viscosity	$[m^2/s]$
υ_S	Sub-grid eddy viscosity	$[m^2/s]$
υ_T	Turbulent eddy viscosity	$[m^2/s]$
ξ	Gaussian random number	$[-]$

1

Introduction

In this chapter the project will be introduced. The background covers why contamination of a side view Camera Monitoring System (CMS) is a problem and why the device is at all necessary. The chapter presents the soiling of a conventional side view mirror, linking it as a basis of understanding for the soiling of a CMS. Subsequently the purpose will be defined, together with the scope, limitations and societal considerations of the project.

1.1 Background

The World Health Organisation estimates that around 1.3 million lives are lost annually due to traffic collision and another 20 - 50 million people suffer injuries, some incurring permanent disabilities [1]. Crashes also cause substantial economic losses through damage on road, vehicle and people. In addition, there is an economic toll due to the significant loss of productivity of deceased or disabled victims [1]. The largest risk factors leading to accidents are flaws in the vehicle, road infrastructure and most significantly, human errors.

According to a report by the Swedish Arbetsmiljöverket, 90% of vehicle accidents may be attributed to human errors [2]. Humans have poor reference for high velocities and poor vision in darkness, fog, glares etc. Humans may also be influenced by emotions such as impulsivity, repression to risks, pride and distractions [2]. To prevent accidents by reducing the human error, modern cars are equipped with advanced safety systems.

1.1.1 Car Safety Systems

Airbags or seatbelts are examples of traditional passive safety equipment that reduce the damage taken to the driver or passenger but do little to prevent accidents from occurring. Cruise control, anti-lock braking and electronic stability control on the other hand take active measures to avoid collisions [3]. These types of active safety systems, illustrated in Fig. 1.1, are often referred to as Advanced Driver Assistance Systems (ADAS), which monitor the vehicles surroundings and detect hazards that are informed to the driver

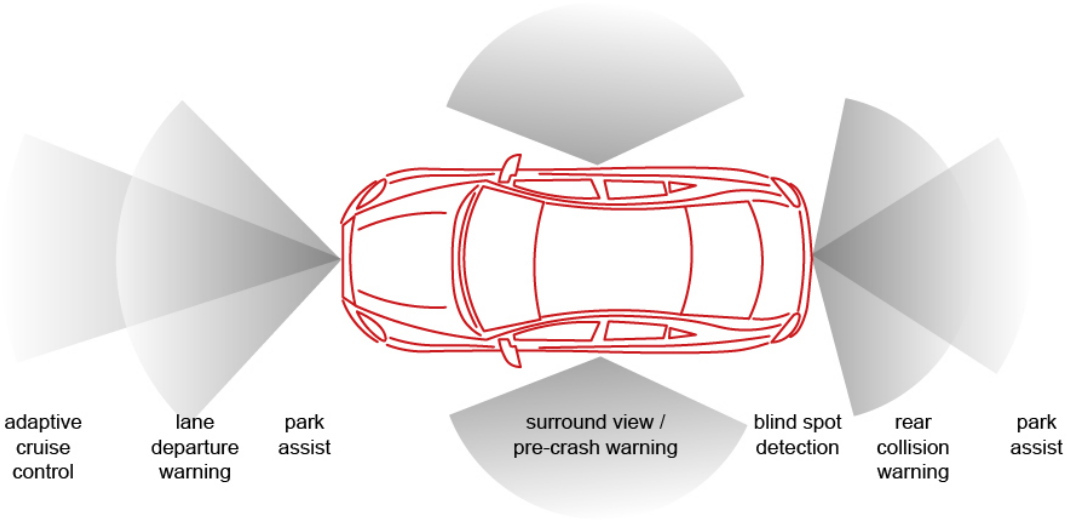

Figure 1.1: *Illustration of various Advanced Driver Assistance Systems, relying on sensors for information [4].*

which have be shown to have a positive effect on traffic safety and contributed to a reduction of collisions. For instance, research using crashing data from insurance companies in Sweden concluded that vehicles equipped with adaptive cruise control experienced 37% fewer rear-end frontal collisions compared the vehicles without such equipment [5, p.1177]. To monitor the vehicle's surroundings, ADAS rely on sensors such as cameras that are increasing in usage [6, p.25].

Figure 1.2: *Exterior view of CMS (L) [7] and interior view of CMS and monitor (R) [8], belonging to an Audi e-tron. Parts of interest are marked.*

1.1.2 Camera Monitoring System

A side view Camera Monitoring System (CMS) is a monitoring equipment which enables both wider side and rear view vision, revealing the driver's blind-spot [9, p.3, 15]. The

CMS consist of an interior monitor which displays the exterior camera's surveillance, retrieved from the camera head attached through an arm to the lateral of the vehicle. The head has a rear-looking face from which monitors the road through a lens. There are examples of modern cars equipped with the camera, such as the Audi e-tron presented in Fig. 1.2.

The CMS can also increase visibility at glaring conditions such as dusk and dawn conditions, and has a generally higher image clarity than a traditional side view mirror [9, p.3, 15–26]. To reduce glare from light pollution, some CMS designs use a glareshield that acts as a wall between the lens and light, an example of which is marked in Fig. 1.2.

These benefits indicate that complementing or replacing side view mirrors with a CMS may lead to a reduction in traffic collisions and contribute to road safety. This however requires that the camera function reliably, which is not guaranteed under all weather conditions as its vision may be obstructed when soiled.

1.1.3 Contamination of a Side View Mirror

Vehicle contamination may be for instance by mud, snow, sand or water. In this project, it was contamination by airborne water droplets that was the main topic. Generally, on-road vehicle water soiling may be assigned to three categories [10]:

- **Self contamination** - Road spray generated by own vehicle's tyre rotation.
- **Third-party contamination** - Road spray generated by another vehicle's tyre rotation.
- **Precipitation** - Rainfall deposition.

If only considering third-party contamination of airborne droplets, a conventional side view mirror is mostly soiled aerodynamically by wake vortexes that forms at the rear of the mirror as the vehicle moves [11, p.2, 3].

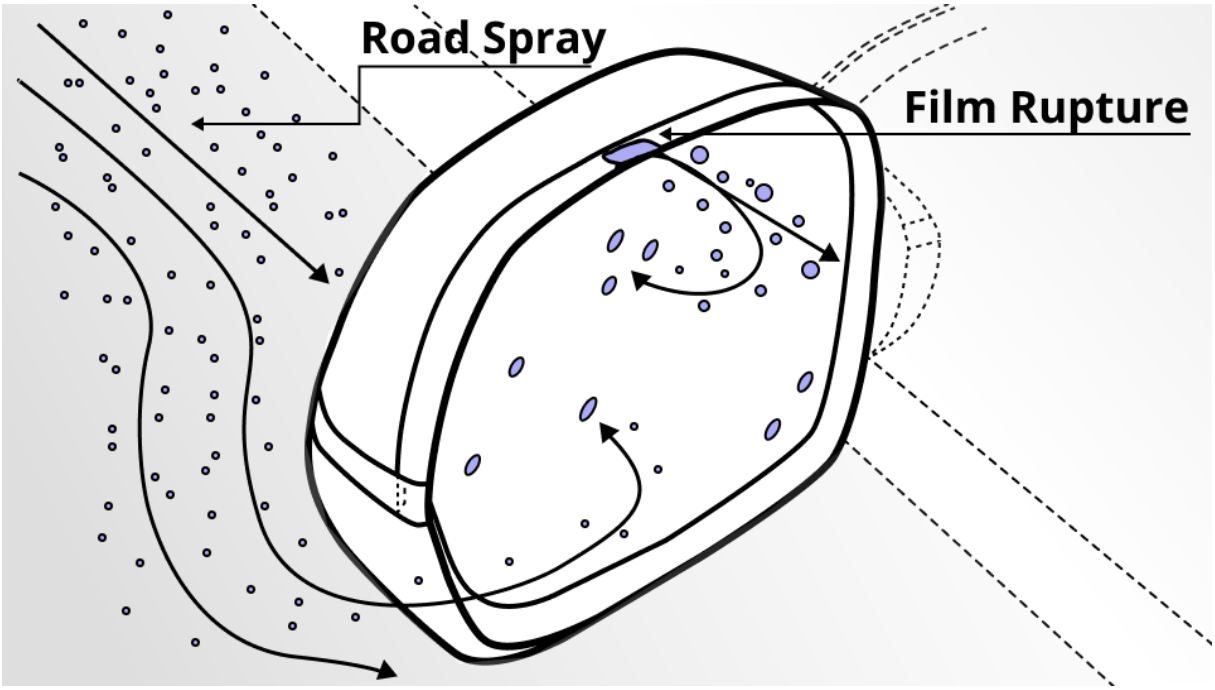

Figure 1.3: *Illustration contamination of a side view mirror by airborne droplets from road spray through droplet entrapment and film rupture. Arrows symbolize trajectory of droplets*

Fig. 1.3 illustrates how airborne droplets suspended by a frontal vehicle's road spray in vicinity to the side view mirror may be entrapped within the reverse flow of the wake, collide and stick to the mirror. As the velocity of the vehicle increases the wake become more turbulent which scatters the droplet deposition across the mirror surface which increases the overall contamination [11, p.6].

The droplets that instead collided with front of the mirror are pushed to the edges of its circumference where they accumulate into liquid films due to the high surface tension of water. The film keep propagating until reaching a critical size, when they rupture and release droplets near the mirror wake that are easily entrapped in and redeposited onto the mirror. This secondary spray through film ruptures is suggested to make up half of the overall mirror contamination [11, p.4].

1.1.4 Previous Work

Various numerical approaches have been used when attempting to model vehicle contamination. Commonly for airborne particle contamination is to use Computational Fluid Dynamics (CFD), as was done on snow modelling [12]. Here, a Lagrangian framework was employed which is the chosen approach of this project. As for water soiling, attempts have been made to simulate the film propagation dynamics [13] and the airborne droplet dynamics [11] using CFD. All these works have compared computational results to experimental obtained in a wind tunnel.

1.2 Purpose

The main purpose of this project is to increase the understanding of CMS contamination by airborne water droplets from road sprays using CFD in Simcenter STAR-CCM+ and experiments in Volvo Cars wind tunnel. Related to this, the following questions will be answered:

- What droplet sizes soil the CMS face?
- Will droplets deform and breakup?
- What droplet forces are significant?

in addition, the project aims to evaluate different design features of the CMS based on what is hypothesised to have an impact on the soiling. These features are

- Altering the shape of the glareshield
- Adding a drainage groove
- Aerodynamic streamlining of the CMS arm

it is also desired to investigate if contamination is affected by driving conditions by answering the following

- Will the CMS be more soiled when driving faster?

1.3 Scope and limitations

The scope of the project focuses solely on one optical sensor, the CMS. Furthermore, only third-party contamination is considered. For simplicity, bluff bodies were used instead of a car as testing geometry. Soiling of the CMS face is the exterior of interest, which is separated into a glareshield and lens region. Also, the material of the CMS is assumed to be homogeneous.

The multiphase system is assumed to be one-way coupled, isotherm, incompressible and consisting of air and a dilute population of pure water droplets. The droplets are assumed to be inherently spherical and when colliding with boundaries they are assumed to always stick.

A simplified prototype CMS was designed and used for both simulations and experiments. Different designs would only have one deviating feature from the baseline for simplicity.

Droplets were only injected at two regions, as either frontal road spray or secondary spray through film ruptures. The road spray droplets' size distribution is assumed to be coherent with literature. The film ruptures are assumed to be dominating at the circumference of the CMS face, which is the only simulated secondary injection region. The injected size distribution set based on observations in experiments. Due to the short simulated physical time, the spray rate will be substantially higher compared to reality and differing between injectors.

1.4 Ethical and Societal Considerations

The background for this project is vehicle safety, where it is the ambition that the results will contribute to better safety technology and a subsequent reduction of vehicle collisions and fatalities.

Another consideration is that the methods and results must be critically evaluated and errors transparently communicated, to avoid causing problems due to negligence.

The automotive industry contribute greatly to technological advancements, but also enviormental development through the phasing out of combustion in favor of electric vehicles. However, additional complex features as the CMS may directly increase the enviormental toll through excavation of material such rare earth elements, energy intense production and a composite product difficult to recycle.

By keeping the CMS clean through design, the need for active cleaning is avoided. This is avoids additional components, cleaning agents and energy required for active cleaning, thus preventing environmental toll and additional economic costs.

2

Theory

This chapter presents a compilation of the theory and literature necessary to understand and justify the method, results and conclusions of this project. It consists of an overview of the relevant dynamics of the multiphase system and computational approaches.

2.1 Fluid Dynamics

The transport phenomena of a fluid describes dynamics of the flow through Eulerian continuum mechanics, which models the fluid as a macroscopic continua where the molecule density is uniformly distributed in space [14, p.1, 2]. This is fundamentally preformed in three dimensions through description of the fluid transport through a discrete volume by the governing Navier-Stokes equations [14, p.28].

2.1.1 Navier-Stokes Equations

The isotherm transport of fluid momentum can be described through the conservation principle of the continuity equation and the forces balancing of the equation of motion [14, p.28].

2.1.1.1 Equation of Motion

Newton's second law states that the change of momentum in each spatial direction must be equal to the forces acting in that direction [15, p.20]. For a fluid flow this is defined through the equation of motion

$$\frac{\partial \vec{U_f}}{\partial t} = \nu_f \nabla^2 \vec{U_f} - \frac{1}{\rho_f} \nabla P - \vec{U_f} \nabla \vec{U_f} \ , \tag{2.1}$$

where $\vec{U_f}$ is the instantaneous fluid velocity vector, ρ_f the fluid density, ν_f the kinematic viscosity and P the pressure, expressing the balancing forces for the change in momentum. These are forces of viscous drag, pressure gradient and advection in that order.

2.1.1.2 Continuity Equation

The law of conservation states that mass may be neither created or destroyed, therefore the mass that exits the discrete volume must equal what entered the same element, unless

it accumulates over time [14, p.33, 34]. This is the principle of continuity may be expressed as

$$\frac{\partial \rho_f}{\partial t} = -\rho_f \nabla \vec{U_f} \ , \tag{2.2}$$

which communicates the equality between transport and temporal change of mass. The continuity equation is coupled with the equation of motion Eq. (2.1).

2.2 Computational Fluid Dynamics

Computational Fluid Dynamics (CFD) solves or models Eq. (2.1) and Eq. (2.2) to simulate the motion and dynamics of a flow. The numeric computations and subsequent visualizations are preformed through software such as STAR-CCM+, ANSYS Fluent, OpenFOAM or Preonlab.

2.2.1 The Finite Volume Method

The Finite Volume Method (FVM) computes the flow through discretization of space into a grid consisting of cells, representative as discrete volumes. In principle, the accuracy of the simulation increases with the number of cells, at the price of increased computational times [15, p.34, 35].

2.2.1.1 Spatial Solving

Each of the spatial grid cells solves the fluid's governing equations locally by integration, as described for the equation of motion through

$$\int_{cell} \frac{\partial U_f}{\partial t} dV = \int_{cell} \nu_f \nabla^2 U_f dV - \int_{cell} \frac{1}{\rho_f} \nabla P dV - \int_{cell} U_f \nabla U_f dV \ , \tag{2.3}$$

these integrals are solved by linear interpolating to form a piece-wise decomposition of the flow field, where each piece is a cell. Thus the analytical solutions of the PDEs are approximated through the discretization. Each cell uses the solution from adjacent cells to compute its own local solution with the accuracy evaluated through comparing the solution of adjacent cells [15, p.40-44]. If the accuracy fails to meet a defined tolerance, all calculations will be carried out again, using the previous solutions as initial values. This process is repeated iterative until the solution between iterations agrees. The solution has then converged [15, p.49-51].

2.2.1.2 Temporal Solving

Many flows, especially those with high turbulence, are unsteady and change with time. Thus, each time will have a unique solution that needs to be computed for a complete solution. Similarly to space, the physical time is also discretized into a number of time steps to represent the transient behaviour of the field. Each step may either use a future, past or mixed time-point for computation [15, p.72-77].

Unlike the spatial solvers, the temporal change solution over time, requiring sub-iterations

between steps to converge. The time step must be weighted against stability, something that the Courant number quantifies

$$CFL = U_f \frac{\Delta t}{\Delta x} \ , \tag{2.4}$$

where U_f is the magnitude of fluid velocity, Δx the spatial step size and Δt the temporal step size. When this number exceeds 1, entities may skip cells which can cause instabilities. A smaller CFL resolves a higher resolution of time scales, but if too small, the solution is very slow [15, p.78].

2.3 Turbulence

Turbulence emerges from disturbances to the flow that aren't damped by viscosity, forming swirls and other high orthogonal gradient features originating from the fluid's inertia. Turbulent flows are characterized by unsteady, chaotically fluctuating velocity components in all spatial dimensions that are challenging to fully describe. The relation between disturbing inertial and stabilizing viscous forces is quantified through the Reynolds number

$$Re = \frac{\rho_f U_f l_0}{\mu_f} \ , \tag{2.5}$$

where μ_f is the dynamic viscosity of the fluid and l_0 is a characteristic length scale of the flow [14, p.153, 154]. Flows are kept turbulent through supply of energy which is transferred from the mean flow to the large scale fluctuations, eventually cascading to the smallest scales of turbulence where the energy dissipates into heat through stabilization by viscous stresses [15, p.101].

2.3.1 Turbulence Models

To fully solve all turbulence of a high Re-flow in CFD, a solution to every existing scale of turbulence is required. This puts an extremely high requirement on the grid, as vortexes near boundaries produce very high velocity gradients that require a large number of cells to resolve. Rather, turbulence is commonly either partially resolved or completely modelled.

2.3.1.1 Reynolds Averaged Navier-Stokes

Reynolds Averaged Navier-Stokes (RANS) models the turbulence instead of solving it and is based on the Reynolds decomposition

$$\vec{U_f} = < \vec{U_f} > + \vec{u_f'} \ , \tag{2.6}$$

where $< \vec{U_f} >$ is the mean flow and $\vec{u_f'}$ the temporal fluctuation. The same decomposition into mean and fluctuation is made for P. The model then neglects the fluctuations of these entities, which when applied to the Navier-Stokes equations Eq. (2.1) and Eq. (2.2) produces a nearly closed model, with one term requiring closure. Six unknowns of the coupling between the mean and fluctuations of the flow, the Reynolds Stresses, must be either resolved or modelled [15, p.123-126].

The Boussinesq approximation uses the coupling between fluctuations and mean flow to assume a proportionality. The proportionality constant is based on the proposition that turbulence is a diffusive process, meaning that the stresses can be modelled in analogy to molecular viscosity through a turbulent viscosity defined by turbulent kinetic energy k and its dissipation rate ϵ

$$\nu_T = C_v \frac{k^2}{\epsilon} \ , \tag{2.7}$$

where C_v is a proportionality constant. By solving the transport equations of k and ϵ, the RANS equations are closed. This closure models of RANS is known as the standard $k - \epsilon$ model [15, p.126-133].

2.3.1.2 Large Eddy Simulation

Most of the turbulent kinetic energy is in fact carried by the larger scales of turbulence, which are simpler to with a coarser mesh gird. Large Eddy Simulations (LES) is one approach to resolve the turbulence of the larger scales, down to a defined length scale equal to the size of the local cell [15, p.109-11]. Numerically, the velocity is decomposed in space

$$U_f(x,t) = U_{f,\Delta}(x,t) + u_f(x,t) \ , \tag{2.8}$$

where $U_{f,\Delta}(x,t)$ is the spatially filtered velocity and $u_f(x,t)$ contains the unresolved sub-grid information. This is comparable to the decomposition in RANS (Eq. (2.6)), the difference being spatial decomposition rather than temporal. The acquisition of $U_{f,\Delta}(x,t)$ is achieved through applying a filter function G using a filter width Δ to the spatial dimension of the velocity field

$$U_{f,\Delta}(x,t) = \int\int\int G(x - x'; \Delta) U_{f,i}(x',t) d^3x' \ , \tag{2.9}$$

where x' is the sub-grid length scale [16, p.264, 265]. Again, corresponding decomposition and filtering of P is preformed and is together with $U_{f,\Delta}(x,t)$ used for solving Eq. (2.1) and Eq. (2.2), with the remaining unresolved turbulent length scales being smaller than Δx and modelled using a sub-grid viscosity ν_s [15, p.110].

2.3.1.3 Delayed Detached Eddy Simulation

LES often require unfeasible refinements of the near wall region grids. A solution is to combine LES with RANS which preforms better at these regions. In practice, this means that the attached eddies will be modelled through RANS and the detached eddies of regions with flow separation will be partially resolved through LES. This hybrid simulation method is one example of a Detached-Eddy Simulation (DES). The models considers a length parameter $\tilde{d}$ used for adjustment of modelled viscosity. It is computed by comparing the nearest distance to a boundary with the largest grid spacing on the local cell

$$\tilde{d} = min(d, C_{DES}\Delta) \ , \tag{2.10}$$

where C_{DES} is a dynamic constant which is usually within the order of magnitude of 1. Thus, when $d << \Delta$, the eddy viscosity of RANS is used and when the grid is fine enough,

with $d >> \Delta$, The sub-grid viscosity model of LES is used [17, p.4, 5].

It may be desired to override the length criteria and enforce RANS regardless of boundary region grid resolution [18, p.181]. This approach is the Delayed Detached Eddy Simulation (DDES) and is formulated with a correction to Eq. (2.10)

$$\tilde{d} = d - \mathcal{F}_d \; max(0, d - C_{DES}\Delta) \; , \tag{2.11}$$

where $\mathcal{F}_d$ is a function designed to be 1 in LES regions and 0 elsewhere, which also provides the desired property of retaining RANS in certain regions [18, p.184, 185].

2.3.2 Wall Theory

As already inquired from Section 2.3.1.3, near wall regions pose a great computational challenge to properly simulate. This is due to adverse velocity and pressure gradients arising from the no-slip condition, a concept that will be discussed in this section.

2.3.2.1 Boundary layers

Viscous flows experience resistance to inertial deformation through transport of momentum that dissipates at a boundary, forming the no-slip condition that states that the velocity relative to an adjacent boundary is zero [14, p.83]. This slows the fluid in the near boundary regions, forming a boundary layer where the velocity in direction of the flow gradually is reduced as the distance to the wall decreases. This layer may be either laminar, turbulent or transitional depending on Re in the boundary regions. As with turbulence in general, the turbulent layers are challenging to predict, but may be decomposed into two regions, an outer region of gentler shear and an inner with strong gradients [15, p.147].

The inner region is illustrated in Fig. 2.1 as a function of the shear velocity $U_{f,y}$. The inner-most viscous sub-layers (I) is dominated by viscous stress where turbulent kinetic energy dissipates into molecular heat. At some distance from the boundary, within the buffer sub-layer (II) both viscous and turbulent stresses are significant with the former fading as the distance increases, until at the fully turbulent sub-layer (III) where turbulent shear stress dominates completely [15, p.148].

The distance to the wall is commonly evaluated in its dimensionless form

$$y^+ = \frac{y_w}{\nu_f}\sqrt{\frac{\tau_w}{\rho_f}} \; , \tag{2.12}$$

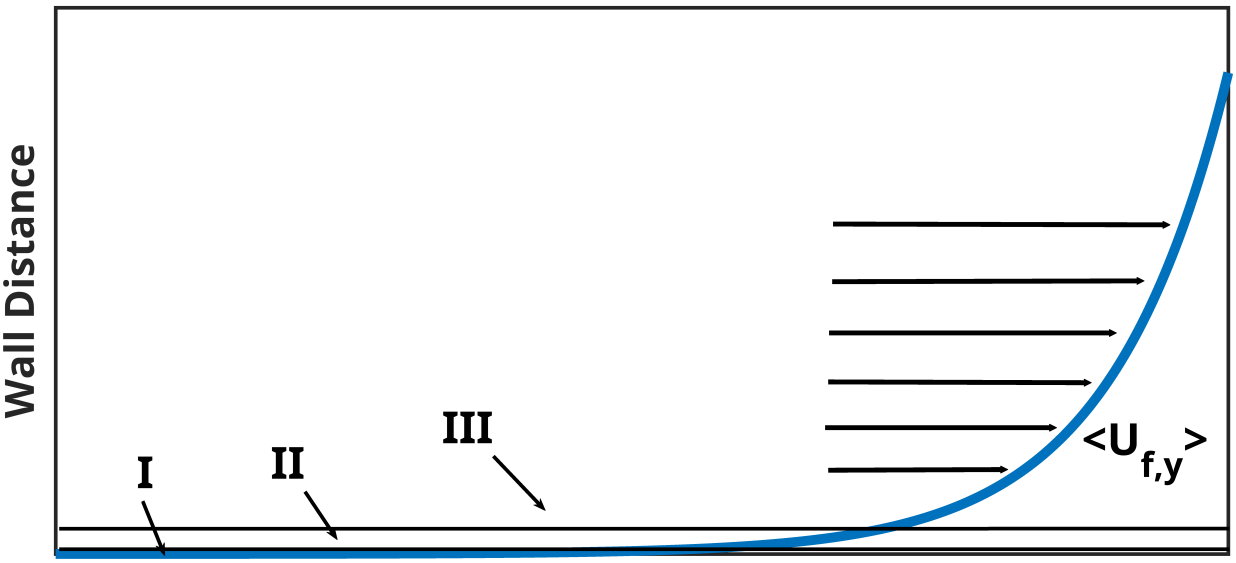

Figure 2.1: *Inner region of a turbulent boundary layer, with the corresponding shear velocity profile at distances to the wall. The three sub-layers are marked.*

where y_w is the wall distance and τ_w is the shear wall stress. The advantage of this formulation is that the dimensionless form is general for most flows [15, p.148-149].

2.3.2.2 Wall Models

In CFD, the turbulent boundary layer is difficult to adequately capture with the mesh. One common way to handle these regions is the high y^+-approach which applied the law of the wall, illustrated in Fig. 2.2. The law estimates the transport entities such as the dimensionless mean friction velocity $< U >^+$ in the first cell adjacent to the wall [15, p.151]. The law states that $y^+ = < U >^+$ at I, while at III $< U >^+$ may computed through the wall function

$$< U >^+ = \frac{1}{K} ln\ y^+ + B\ , \tag{2.13}$$

where K is the von Kármán constant and B an intersection constant. To successfully avoid the high gradient region of II, the wall functions should be applied at $100 > y^+ > 30$, meaning that the first grid point is placed at $y^+ = 100$ [15, p.152-156].

The low y^+ approach instead uses a refined mesh in within the boundary layer. It requires at least 10 grid points in I, placing the first one close to $y^+ = 1$. To account for the adverse turbulent properties damping functions are added to the ϵ transport equation used in $k - \epsilon$ RANS [15, p.161- 63].

The all y^+-approach combines both approaches and applies the high y^+-approach when the boundary layer grid is too coarse and the low y^+-approach when it's sufficiently fine.

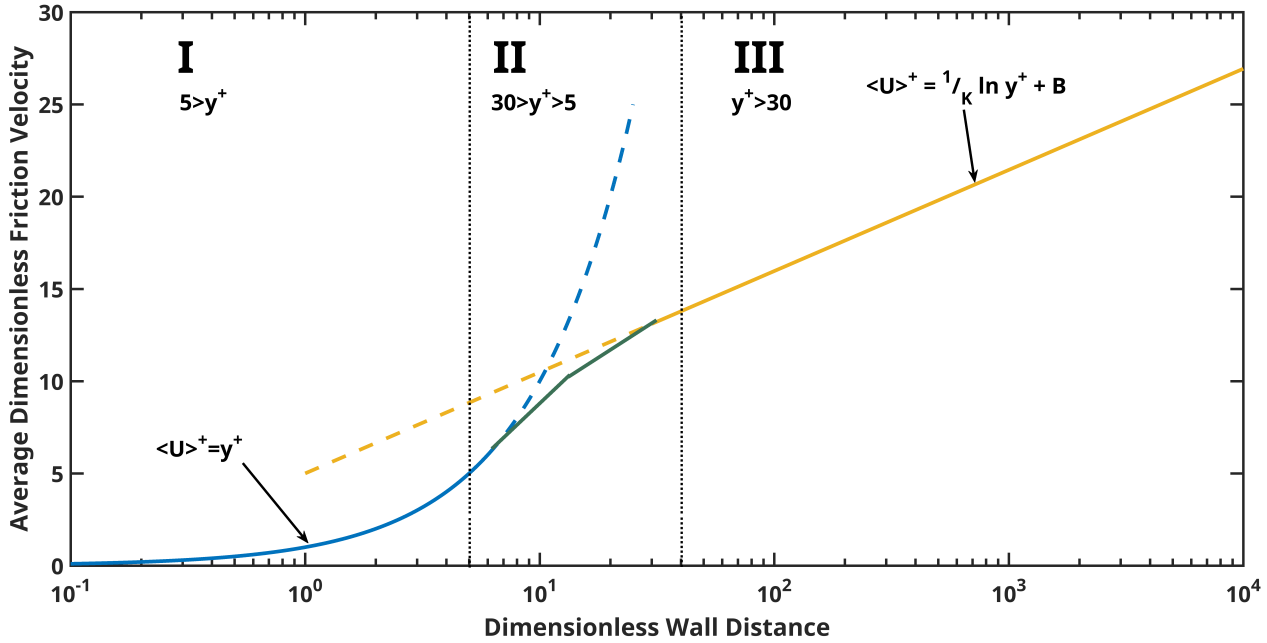

Figure 2.2: *The law of the wall with respect to the average dimensionless friction velocity, the three layers of the turbulent boundary regions inner layer are marked.*

2.4 Droplet Equation of Motion

As with the fluid flow, the motion of airborne droplets may be described through Newton's second law

$$m_p \frac{dU_p}{dt} = \sum F_i \ , \tag{2.14}$$

where m_p is the mass of the particle, U_p its velocity magnitude and F_i the particle force magnitude of force i [15, p.245, 251]. In one-way coupled, dispersed and dilute multiphase flows where the particles are airborne water droplets, some forces are usually neglected. For instance, buoyancy due to the high difference in density between phases may be ignored, introducing an error of no more than 0.1% [19, p.46]. Thus, the droplets' motion is proposed to be balanced by

$$m_p \frac{dU_p}{dt} = F_G + F_D + F_P + F_L + F_{VM} \ , \tag{2.15}$$

where the subscripts denote gravity, drag, pressure gradient, shear lift and virtual mass in that order. Fig. 2.3 illustrates these forces acting on a droplet in motion with a diameter d_p. The diameter is the most defining parameter for characterization of the droplet behaviour, as all properties and dynamics depend on its size [19, p.8]. Therefore, all the proposed forces will be defined through functions of d_p in the following sections.

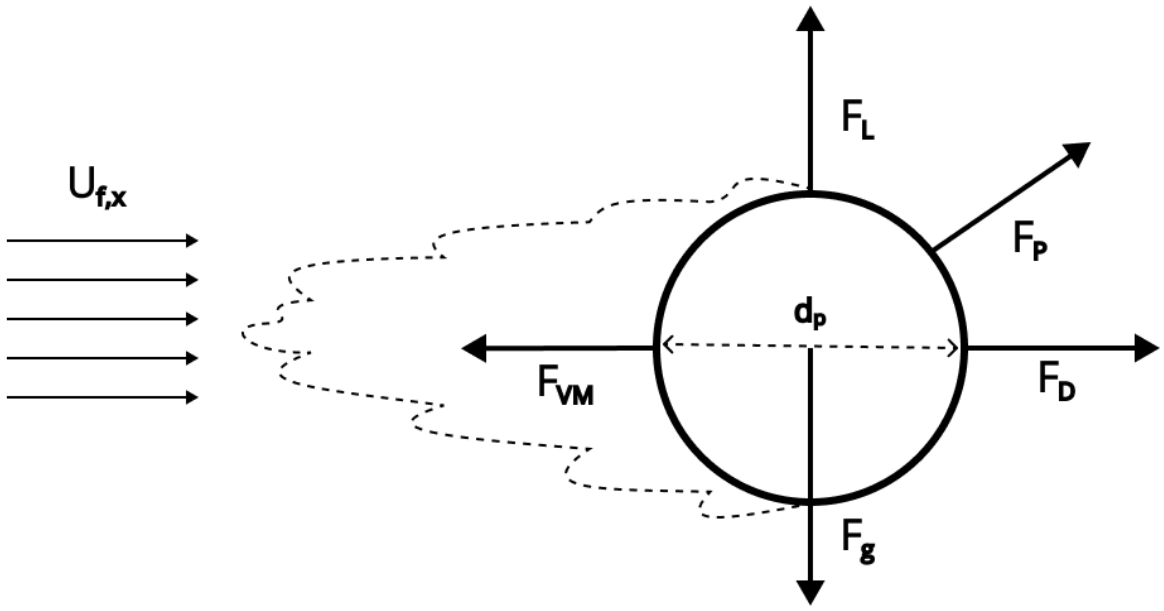

Figure 2.3: *Illustration of proposed relevant forces acting on a droplet with diameter d_p in air, assuming a diagonal pressure gradient.*

2.4.1 Gravity

The force acting on a particle's center of mass due to gravity is

$$F_g = \frac{\pi \rho_p d_p^3}{6} g \ , \tag{2.16}$$

where ρ_p is the droplet's density and g is the gravitational constant.

2.4.2 Drag

For a particle in motion the resistance by the air is a result of the acceleration of the displaced air and friction. The acceleration is proportional to the relative velocity between the particle and the air, a proportionality that defines the drag force experienced by a spherical particle in motion

$$F_D = C_D \frac{\pi}{8} \rho_f d_p^2 |U_f - U_p| (U_f - U_p) \ , \tag{2.17}$$

where C_D is the coefficient of drag [19, p.42, 43]. C_D depends on the viscous regime of the flow surrounding the particle, which is quantified through the particle Reynolds number

$$Re_p = \frac{\rho_f d_p |U_f - U_p|}{\mu_f} \ . \tag{2.18}$$

When $Re_p < 1$ and viscosity dominates the flow is within the regime of Stoke's law. The law states that since flow surrounding the particle is laminar, F_D arises from fluid friction.

When $Re_p >> 1$ and the flow surrounding the particle is turbulent, Newton's Resistance law better describes F_D which states that C_D is constant when inertia dominates [19, p.42-45].

The Schiller-Neumann correlation is commonly used to compute C_D by applying the Re_p regimes [15, p.263]

$$C_{D,sphere} = \left\{ \begin{array}{ll} \frac{24}{Re_p} & \text{if } Re_p < 0.5 \\ \frac{24}{Re_p}(1 + 0.15Re_p^{0.687}) & \text{if } 0.5 < Re_p < 1000 \\ 0.44 & \text{if } Re_p > 1000 \end{array} \right\} , \tag{2.19}$$

which is valid for a spherical particle. However, a droplet deformed by aerodynamic forces will no longer be spherical, which is explained further in Section 2.5. The deviation from spherical can be included through Liu's correlation, which interpolates between spherical and the distorted disc-shaped drag coefficients

$$C_D = (1 + 2.632y)C_{D,sphere} , \tag{2.20}$$

where $1 > y > 0$ is the distortion interpolation parameter and $C_{D,sphere}$ is the drag coefficient obtained from Eq. 2.19 [20, p.380].

2.4.3 Pressure Gradient

When significant differences in the fluid's pressure act over the droplet surface, the droplet is accelerated in the direction of the gradient. The force may be described as

$$F_P = -\frac{\pi d_p^3}{6}\nabla P , \tag{2.21}$$

where ∇P is the fluid pressure gradient [15, p.246].

2.4.4 Shear Lift

Similarly to F_P, orthogonal fluid velocity gradients typically found in vortexes act over the volume of the particle which may accelerate it in the direction of the gradient [15, p.247]. The lifting force may be described as [21]

$$F_L = C_L\frac{\pi}{8}\rho_f d_p^3|(\vec{U_f} - \vec{U_p}) \times \vec{\omega}_f| , \tag{2.22}$$

where C_L is the shear lift coefficient, $\vec{U_f}$ the fluid velocity vector, $\vec{U_p}$ the particle velocity vector and $\vec{\omega}_f$ is a fluid vortex's curl vector. Note that prior to computing the vector magnitudes, the crossproduct $(\vec{U_f} - \vec{U_p}) \times \vec{\omega}_f$ must be calculated. F_L is characterized by two dimensionless numbers, Re_p defined in Eq. (2.18) and the shear Reynolds number

$$Re_S = \frac{\rho_f d_p^2 \omega_f}{\mu_f} \tag{2.23}$$

where ω_f is the magnitude of the fluid vortex's curl. C_L may be described through the Summerfeldt correlation [22, p.20, 21]

$$C_L = \frac{4.1126}{Re_s^{0.5}} \mathscr{F}(Re_p, Re_s) \ , \tag{2.24}$$

with the correction factor

$$\mathscr{F}(Re_p, Re_s) = \left\{ \begin{array}{ll} (1 - 0.3314\beta^{0.5})e^{-0.1Re_p} + 0.3314\beta^{0.5} & if \quad Re_p \leq 40 \\ 0.0524(\beta Re_p)^{0.5} & if \quad Re_p > 40 \end{array} \right\} \ , \tag{2.25}$$

and with

$$\beta = 0.5\frac{Re_s}{Re_p} \ . \tag{2.26}$$

2.4.5 Virtual Mass

When a particle accelerates through a fluid, there is a corresponding fluid acceleration which adds an apparent mass to the particle. The added virtual mass contributes to the momentum of the particle which is proportional to the displaced fluid mass and the relative acceleration of the phases

$$F_{VM} = \frac{1}{12}\rho_f d_p^3 \frac{D}{Dt}(U_f - U_p) \ , \tag{2.27}$$

this force is the opposite force of drag as it acts from particle on fluid [16, p.91-93]. This mass is usually neglected when the added mass is small relative the particle mass or when the density difference between phases is high [15, p.246].

2.4.6 Lagrangian Point-Parcel Approach

In CFD, the motion of airborne droplets may be simulated by individual tracking or as bundled parcels. This is the Lagrangian Point-Particle Approach and for a one-way coupled system it has the computational advantage that the particles can be tracked post-processly as they do not influence the flow [15, p.244, 250, 251]. In this project, parcels will be referred to as particles or droplets. As the fluid properties such as velocity, vorticity and pressure is retrieved, the particles motion may solved through integrating the trajectory based on their current position

$$\frac{d\vec{x}_p}{dt} = \vec{U}_p \ , \tag{2.28}$$

where $\vec{x}_p$ is the particle's position and $\vec{U}_p$ is obtained by solving the particle's motion (2.14).

One significant drawback with this approach is the exclusion of unresolved turbulence as the modelled viscosities from RANS or LES don't add momentum to the particle. The small scale velocity fluctuations by turbulence may chaotically affect F_D, changing U_p and the particles direction. The discrete-random-walk model adds a random velocity

component for the same time T the particle have spent in a turbulent scale of length l. This time is estimated as the minimum passing time and the life time of the scale

$$T = -\tau_p \ln(1 - \frac{l}{\tau_p |U_p - < U_f >|}) \ , \tag{2.29}$$

where τ_p is the particle response time. The turbulent velocity fluctuations are sampled from a Gaussian probability distribution and the turbulent fluctuation are added to the fluid velocity

$$\vec{u}'_f = \xi \sqrt{\vec{u}'^2_f} \ , \tag{2.30}$$

where ξ is a Gaussian random number and the derivation of l from $\vec{u}'$ depending on turbulence model [15, p.252-254].

2.5 Droplet Integrity

When subjugated to aerodynamic forces, airborne droplets may lose their integrity and be deformed, eventually fragmenting into smaller droplets as illustrated in Fig. 2.4.

In addition to the external forces affecting the motion of the droplet, there are also internal forces maintaining the integrity of the spherical droplet. The high surface tension of water is a molecular phenomena which resists the deformation and drives the shape back to spherical as the water molecules favors attractions to one another [14, p.12, 13]. The sizing of aerodynamic inertia versus surface tension is quantified through the Weber number [20, p.372]

$$We = \frac{\rho_p (U_f - U_p)^2 d_p}{\sigma_p} \ , \tag{2.31}$$

where σ_p is the surface tension of water. While σ_p is the most significant opposition to deformation, the viscosity of the droplet dissipates the supplied kinetic energy by the distorting forces, contributing to the integrity of the droplet. The Ohnesorge number sizes viscosity and surface tension [20, p.372]

$$Oh = \frac{\mu_p}{\sqrt{\rho_p d_p \sigma_p}} \ , \tag{2.32}$$

where μ_p is the particle viscosity. In this section, the mechanisms of droplet deformation and breakup will be described through these numbers.

2.5.1 Deformation

As a droplet deforms, its spherical shape is stretched into an ellipsoid shape with a cross sectional surface aligned with the flow direction as seen in Fig. 2.4. One method to estimate maximum deformation of the droplet before breakup is through the Hsiang and Faeth correlation [20, p.380], valid at $We < 100$ and $Oh < 0.1$,

$$(\frac{d_{def}}{d_p})_{max} = 1 + 0.19 We^{1/2} \ , \tag{2.33}$$

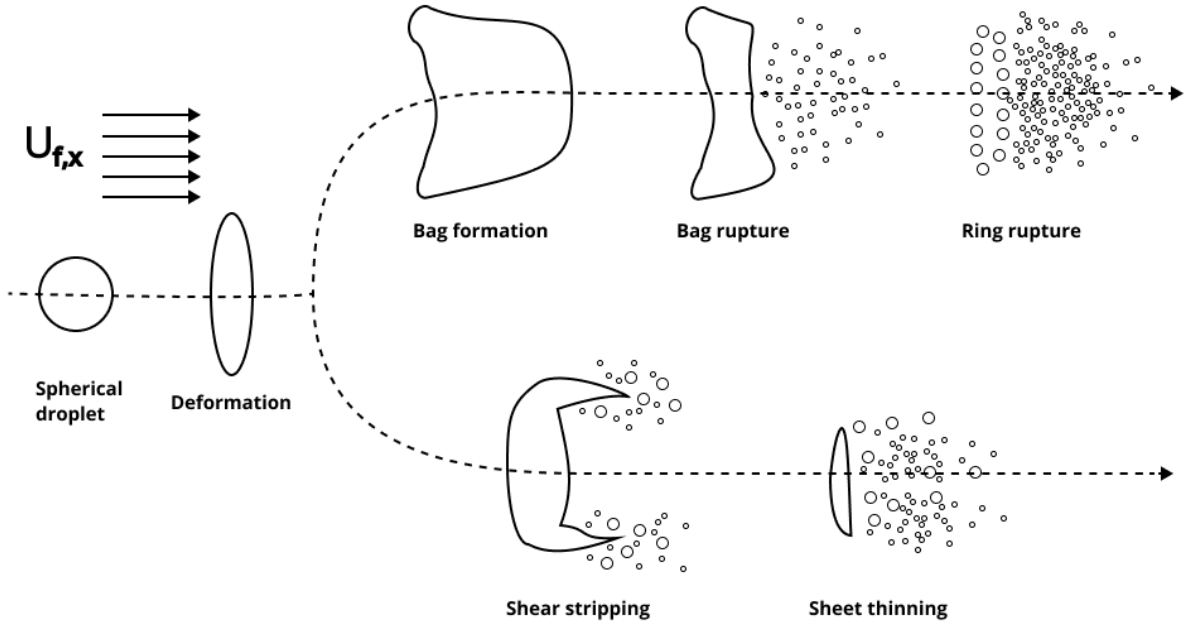

Figure 2.4: *Illustration of deformation and two low Weber number breakup modes of a droplet subjugated to aerodynamic forces, either bag-breakup or shear-stripping.*

where d_{def} is the deformed disc-like diameter.

2.5.2 Breakup Modes

As deformation progresses and We increases, the center of the droplet is blown downstream, forming a hollow "bag" attached to a ring as seen in top row of Fig. 2.4. Eventually the bag bursts and fragments in to a large number of small droplets. Finally, the ring also bursts into a smaller number of larger fragments [20, p.380, 381]. This is the bag-breakup mode and if $Oh < 0.1$ it initiates at $We = 11$, dominating within $11 < We < 35$ [20, p.377].

At higher We, the air flow forms a boundary layer on the droplet surface due to it's shear. At the peripheries of the droplet, the layer is unstable and strips it of mass forming smaller fragments, as seen in the bottom part of Fig. 2.4. Eventually, the entire droplet has been stripped. This is shear-stripping, which dominates at roughly $We > 80$ [20, p.377, 382]. Between the ranges of bag-breakup and shear-stripping is a transitional regions where both modes are possible.

2.5.3 Integrity Models

The computational modelling of droplet deformation and breakup used in CFD differs depending on situation, but for a airborne water spray the following proposed models are commonly employed.

2.5.3.1 Taylor Analogy Distortion and Breakup

The Taylor analogy breakup (TAB) models the droplet distortion as a damped spring-mass system, with the distortion represented by the displacement and the rate of distortion by the velocity of displacement. The deformation x_{dis} is expressed as TAB displacement y_{TAB}, a normalized parameter with

$$y_{TAB} = \frac{2x_{dis}}{C_b d_p} \ , \tag{2.34}$$

where C_b is an empirical constant. As y_{TAB} uses deformation relative local flow direction, it may also be negative. Thus, it is once $|y_{TAB}| > 0$ deformation occurs and at $|y_{TAB}| = 1$ when the TAB breakup model describes fragmentation into smaller, Rosin-Rammler distributed droplets. The TAB model is valid at low We for certain types of sprays [23].

2.5.3.2 Reitz-Diwakar Breakup

The Reitz-Diwakar breakup model doesn't include deformation but may be combined with TAB distortion in STAR-CCM+. The model includes the previously described modes when We increases, by relating the breakup process to a characteristic time scale τ_b. This time scale is used to calculate a stable child droplet diameter D_S and depends on the mode of breakup [24].

2.6 Droplet Inertia

The inertia of a droplet is a property that reduces its responsiveness to changes in the flow [19, p.121]. For instance, the droplet may respond slowly to velocity changes or deviate from curved flow trajectories due to its inertia, forming a nonzero relative velocity

$$U_s = U_f - U_p \ , \tag{2.35}$$

between the phases. The inertia and subsequent U_s increases with the size of the droplet, as illustrated in Fig. 2.5, where it is described how the inertia of airborne droplets in motion may quantified by the Stokes number which compares two timescales

$$Stk = \frac{\tau_p}{\tau_f} \ , \tag{2.36}$$

where τ_f is the characteristic time scale of the flow [19, p.121]. τ_f may be obtained using a characteristic length scale l_0 and the local flow velocity U_f. The acquisition of τ_p differs depending on the viscous regime of the flow surrounding the droplet, as characterized by Eq. (2.18). When $Re_p < 1$ Stoke's law is valid

$$\tau_p = \frac{\rho_p d_p^2}{18\mu_f} \ . \tag{2.37}$$

The droplet with $Stk < 1$ in Fig. 2.5 have curve-linear motion meaning that it responds rapidly to directional gradients and follows the trajectory of the flow. The droplet with

$Stk > 1$ deviates from the curved trajectory and the droplet with $Stk >> 1$ completely ignores the trajectory due to their inertia [19, p.119, 120].

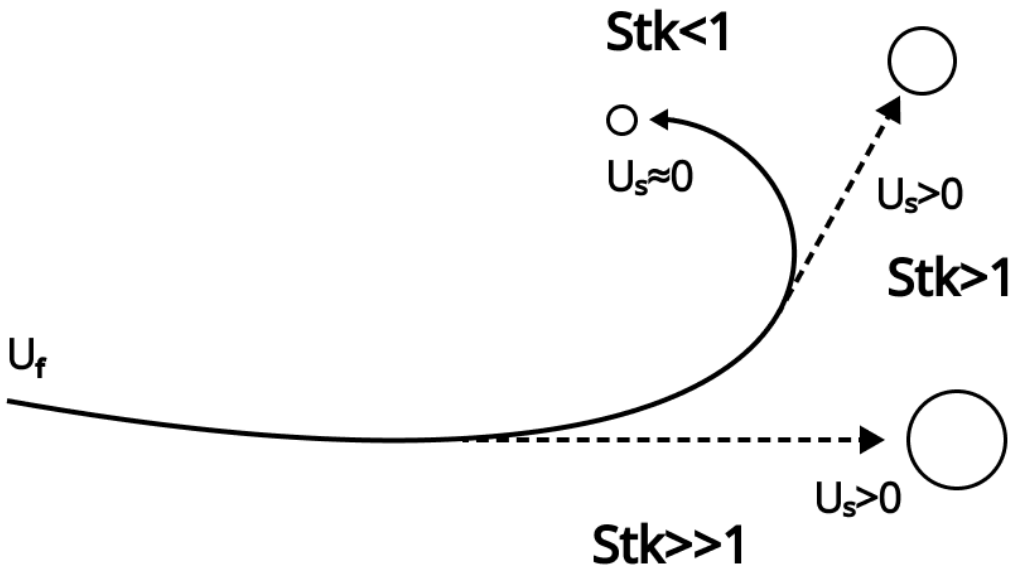

Figure 2.5: *Illustration of droplet inertia when flow trajectory is curved of three different sized droplets all initially following the linear trajectory of the flow.*

3

Method

This chapter presents the general method of the project, with the intent to provide sufficient information to understand how the results were obtained. The outline of the chapter includes a description of geometries used, motivations of choices for particular droplet physics models and the overall CFD-methodology. Experimental setup and method will also be described, as will the preformed trials of experiments and simulations.

3.1 Geometries

Due to desire for simplicity, aerodynamic bluff bodies were used in substitution of a real car for both experiments and simulations. This allowed for considerably faster simulations with simpler flows, enabling a simpler analysis of dynamics and CMS design features. The Wedgeoid was the desired bluff body for all experiments and simulations, however due to its absence in the first wind tunnel experiment, the available Wedge geometry was used for for this experiment and early simulations. For details regarding the Wedge geometry design, see Appendix A.1.

3.1.1 Wedgeoid

Once constructed, the Wedgeoid geometry was used for the majority of simulations and the second experiment (Section 3.2.2). The design aimed to upgrade the original Wedge by attaching a cuboid geometry to the rear and is presented in Fig. 3.1. This would retain the key aerodynamic features of the Wedge and add additional similarities to a car's aerodynamics. The addition of the cuboid enabled additional positions for the prototype CMS which would contribute to providing a simpler flow around the camera while still retaining comparative properties with attachment to a real car.

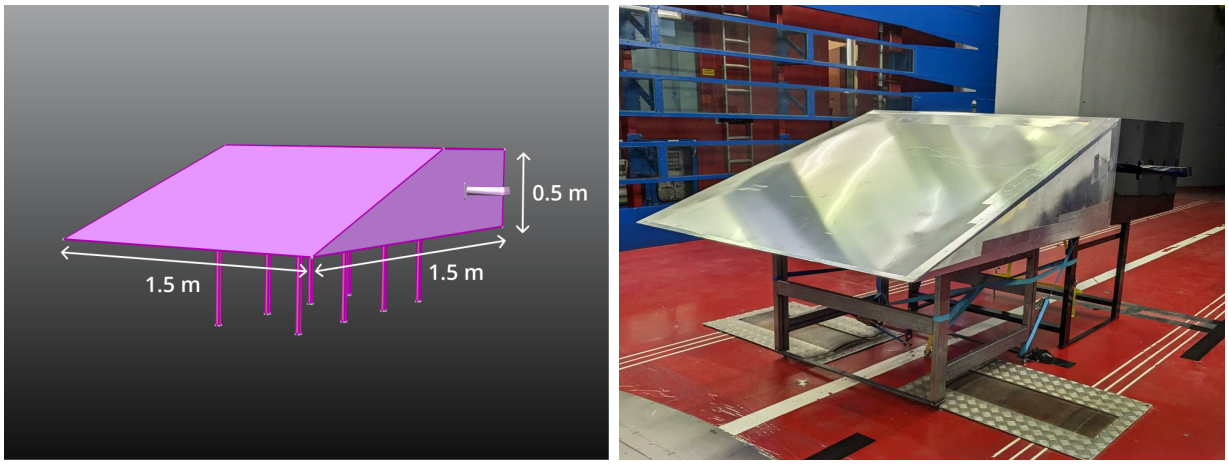

Figure 3.1: *View of Wedgeoid body with attached baseline CMS with dimensions (L) and the real construction in the wind tunnel (R).*

3.1.2 CMS Designs

The prototype was meant as a simplification of a general CMS. It was simplified by removing flow-disturbing features, such as protruding and recessed parts of the exterior. The junction between CMS head and arm was also smoothed to increase the aerodynamic properties. Finally, the material of the CMS was homogenized, making no distinction between for instance lens and glareshield. The baseline CMS design is presented in Fig. 3.2.

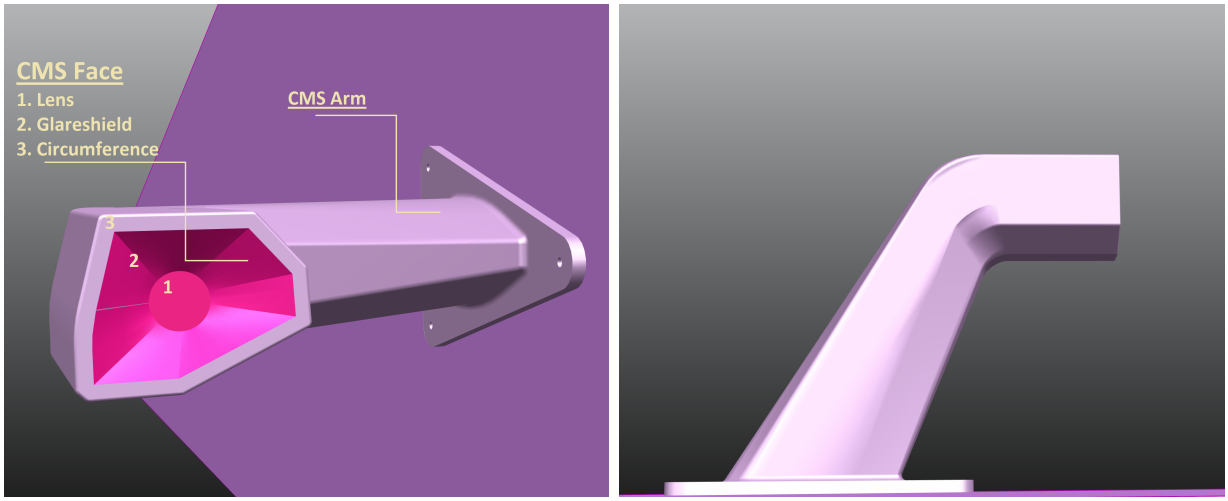

Figure 3.2: *Views of the baseline CMS design attached to the Wedgeoid, with relevant terminology.*

This baseline design would be used for most analysis of fluid and droplet dynamics, with additional designs altering a single feature of the baseline based on observations made from experimental and simulation results. In total, six additional CMS prototypes were designed in CATIA. They were grouped on basis of feature alteration category:

- **Glareshield Group**: Deeper GS, Wider GS and Slanted GS

- **Groove Family** - Basic Groove and Slanted Groove
- **Aerodynamic Alterations** - Aerodynamic Arm

The CMS designs were 3D-printed and coated with car paint to enable cohesive surface properties with a real car.

3.1.2.1 Glareshield Group

To investigate the impact a glareshield has on CMS contamination, three glareshield altering designs were derived, presented in Fig. 3.3. The Deeper GS would double the depth from 10 mm to 20 mm, providing additional cover to the lens by adding distance from spray sources. Similarly, the Enlarged GS design would increase the width by between 40 - 160% depending on glareshield section, which would also cover to the lens. Finally, the Slanted GS design would add a vertical 30^o angle relative the CMS face to investigate if an increased field of view of the camera would expose the lens to soiling.

Figure 3.3: *View of Deeper (L), Enlarged (M) and Slanted GS designs (R).*

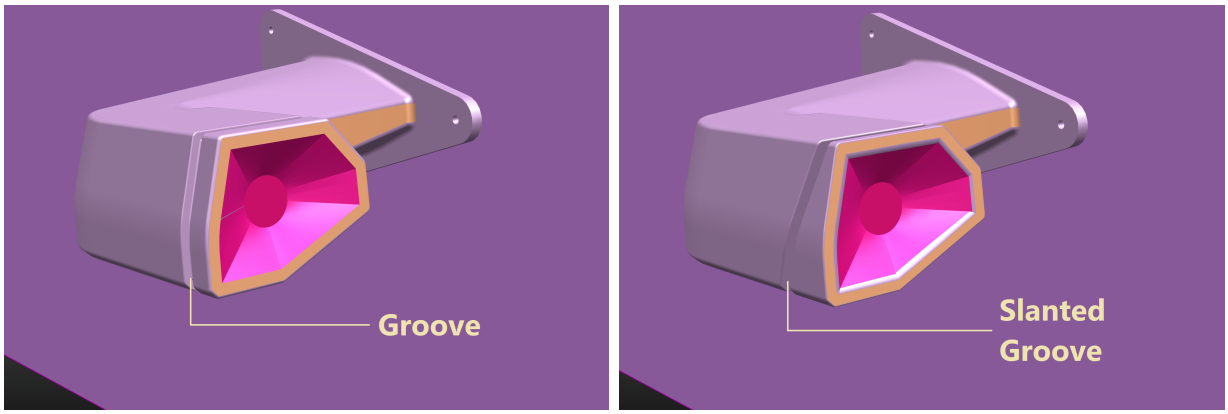

Figure 3.4: *Basic Groove (L) and Slanted Groove(R) designs.*

3.1.2.2 The Groove Family

It was also desired to investigate the impact of a drainage groove, similar to what is present on side view mirrors. Thus, the groove family designs were derived, as presented in Fig. 3.4. Ideally, the Basic Groove design would capture all droplets migrating toward the CMS face and lead them to the bottom patch of the groove, where film ruptures would occur outside the CMS wake and as such not soil the face. The Slanted Groove designed was derived that would use a 28^o angle relative the Basic Groove on the lateral sides of the CMS, aiming at adding additional distance between the film ruptures at the bottom groove batch and wake.

3.1.2.3 Aerodynamic Alterations

From simulation results (Fig. 4.1), it was noted that an additional wake would form at the arm of the CMS that was believed to interact with the CMS face wake to increase its size. Thus, the Aerodynamic Arm design was derived which attempted to streamline the flow at the arm by flattening it into a more aerodynamic shape, as presented in Fig. 3.5. This could avoid the formation of the arm's wake and subsequently reduce the size of the CMS wake, possibly preventing a portion of droplet entrapment.

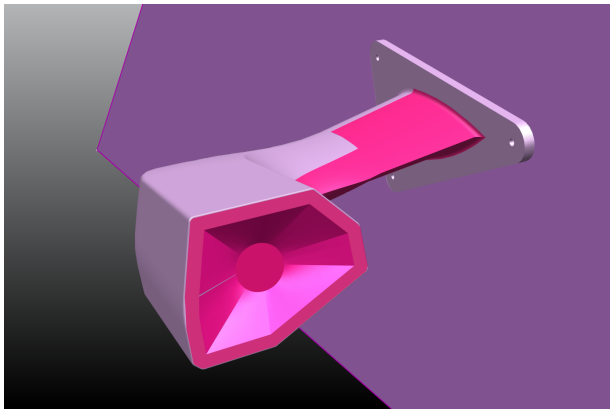

Figure 3.5: *Aerodynamic Arm design.*

3.2 Experimental Method

Two experiments were conducted in Volvo Cars Aerodynamic Wind Tunnel, exposing the bluff bodies and CMS prototypes to different driving conditions. The initial Wedge experiment would be used to derive the CMS designs and CFD methods, see Appendix A.2. The observations made from the second experiment using the Wedgeoid would be used as comparative references to the simulation evaluation of the CMS designs. In this section, the experimental setup and method will be described.

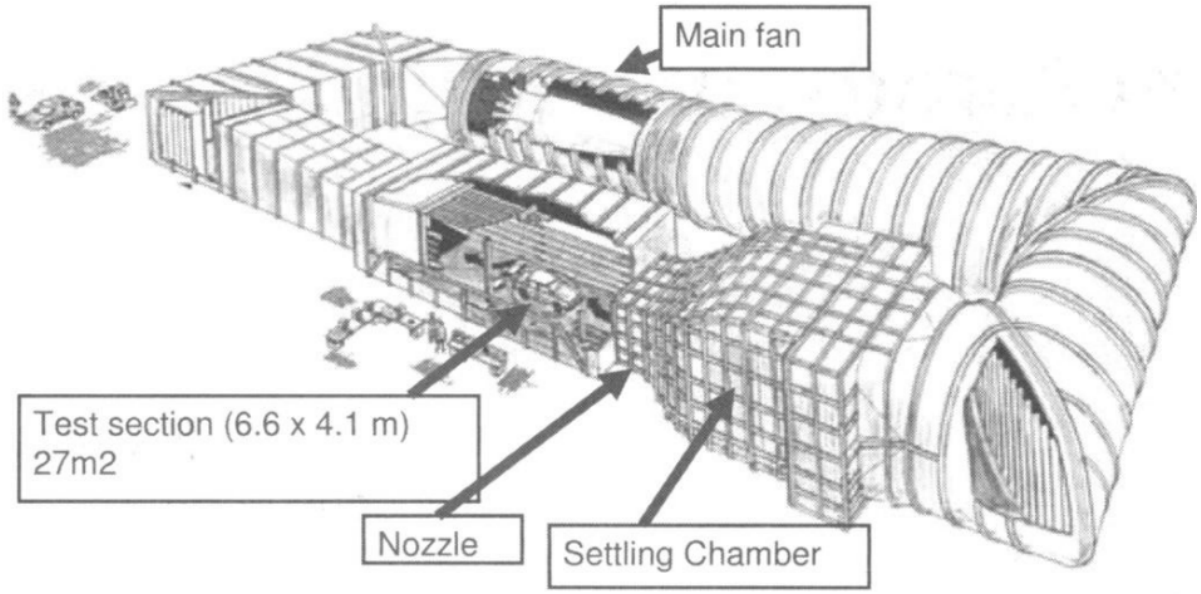

Figure 3.6: *Overview of VCC's wind tunnel with various parts highlighted [25, p.1090].*

3.2.1 Volvo Cars Aerodynamic Wind Tunnel

Volvo Cars wind tunnel is a construction meant to reproduce aerodynamic driving conditions by accelerating the air to create a relative velocity to the test object. The air flows at the immobile test object and is circulated back to its origin by curved plates at the corners of the tunnel. An overview of the tunnel is presented in Fig. 3.6 where four sections are highlighted:

- **Main fan** - Generates the air current of various velocities
- **Settling chamber** - The irregular flow is calmed and turbulence suppressed
- **Nozzle** - Accelerates the air to target velocity
- **Test section** - Location where test body is positioned, cross section on 27 m^2

For soiling experiments, droplets are injected through a spray positioned between the test object and nozzle sections. The spray mixes water and a UV-liquid which illuminates the droplets when exposed to UV-light, enabling visual identification of soiling.

3.2.2 Wedgeoid Experiment

The main experiment conducted in the wind tunnel would test all CMS designs. The experiment would be setup by positioning the Wedgeoid at the center of the test section as presented in Fig. 3.7. Two cameras were positioned and would record each trial and take snapshots, one positioned to capture the back of the prototype CMS and one to capture the front, their views are presented in Fig. 3.8.

Figure 3.7: *Views of Wedgeoid with attached baseline CMS in wind tunnel.*

Figure 3.8: *Frontal and rear view of recording camera on the baseline CMS.*

Trials would be run for 5 minutes with the CMS designs attached to the driver's side of the Wedgeoid, at roughly 2.85 m away from the nose and 0.21 m away from the top. Table 3.1 presents the trials that produced the results used in this report.

Table 3.1: *Trials of Wedgeoid experiment.*

Test	CMS Design	Velocity
1	Baseline	70 km/h
2	Baseline	70 km/h
3	Baseline	70 km/h
4	Baseline	90 km/h
5	Baseline	120 km/h
6	Deeper GS	70 km/h
7	Enlarged GS	70 km/h
8	Slanted GS	70 km/h
9	Basic Groove	70 km/h
10	Slanted Groove	70 km/h
11	Aerodynamic Arm	70 km/h

3.3 Droplet Physics Models

The Lagrangian approach uses Newton's second law (Eq. (2.15)) to resolve the motion of the droplets. In this section, model choices affecting the motion of droplets will be proposed based on droplets' estimated system properties.

3.3.1 Inertia

It was desired to estimate droplets' response to the flow in the CMS wake region and how it related to d_p. Stk was estimated through Eq. (2.36), using the characteristic time τ_f for the flow to pass the CMS face wake. With $U_{f,x} = 70\ km/h$ and the estimated vertical wake length $l_0 \approx 0.024\ m$

$$\tau_f = \frac{l_0}{U_{f,x}} = 0.0012\ s\ . \tag{3.1}$$

For τ_p, it was first desired to investigate the viscous regime of droplets. Through Eq. (2.18) the possible Re_p of the system could be estimated, derived as functions of d_p and U_s, with the ranges $30 > U_s > 0\ (m/s)$ based on simulation results and with $3000 > d_p > 1\ (\mu m)$ based on literature and experimental observations (Fig. A.3). This together with estimations of Stk for the possible velocities at the wake $20 > U_{f,x} > 0\ (m/s)$ are presented in Fig. 3.9. For most droplets within the wake with $U_s > 0$ will likely also have $Re_p >> 1$, the used Stk may provide mostly inaccurate estimations of inertia. It was however the ambition to still consider it for higher Re_p as an indicator of the size range where inertia starts to dominate. The general remark would be that if larger droplets travel with the flow, they are expected to ignore the reverse flow of the wake.

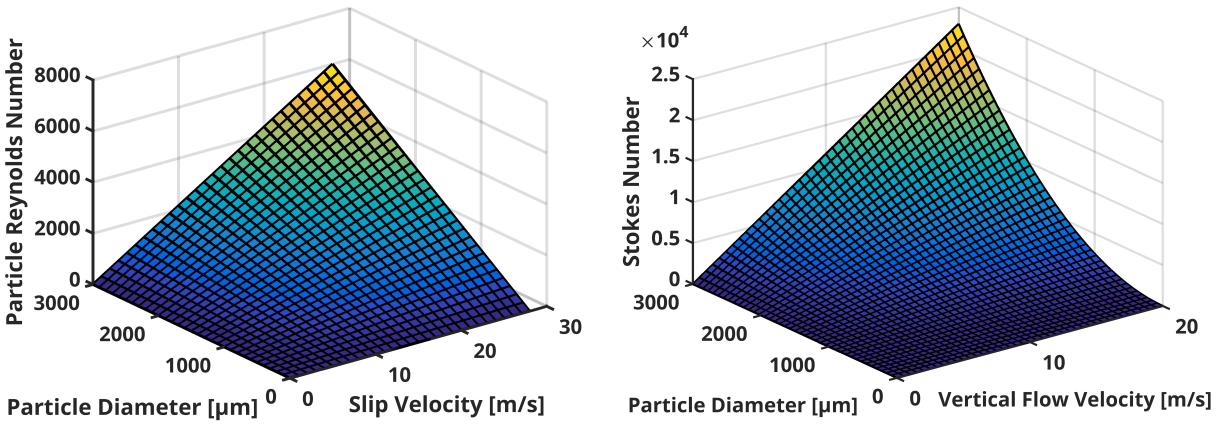

Figure 3.9: *Particle Reynolds numbers (L) and Stokes numbers (R) of the system.*

However, the droplets originating from road spray and not film ruptures are estimated to be within $150 > d_p > 10\ (\mu m)$ and in the near wake region of the main flow where $l_0 = 0.024\ m$ is valid, $Stk = 1$ when $d_p \approx 20\ \mu m$ at which $Re_p < 1$ when $U_s < 0.7\ m/s$. This indicates that Stoke's Law may be valid to determine that road spray droplets with

$d_p < 20\ \mu m$ that are following the main flow adjacent to the CMS wake are expected respond to the wake and perhaps even reach the CMS face, and larger droplets will ignore the wake as illustrated in Fig. 2.5.

3.3.2 Forces

To investigate what forces were relevant for Lagrangian model, the force model equations of Section 2.15 were used to estimate their magnitudes. The examined forces were F_D, F_P, F_g, F_L and F_{VM}. Similarly to buoyancy, F_{VM} was deemed insignificant due to $\frac{\rho_p}{\rho_f} \approx 800$, indicating that the added air mass is small compared to m_p.

The other forces were evaluated as functions of the droplet or flow property they depend on using the same range of d_p and U_s as Fig. 3.9. It should be noted here that the Schiller-Neumann C_D-correlation was used for F_D. For F_P a range of $100 > |\nabla P_{static}| > 0$ (kPa/m) was selected and for F_L a range of $10000 > \omega_f > 0$ (/s) through observations of the simulated fluid fields (Fig. B.3 and Fig. B.4). F_L was more complicated to size as it depends on three variables and the crossproduct of two of them, but was visualized through surfaces of the force against diameter and slip velocity, using a colorbar for the vorticity. The complete estimations are presented in Fig. 3.10. The estimations indicate that all four forces may be significant, thus all were used in simulations.

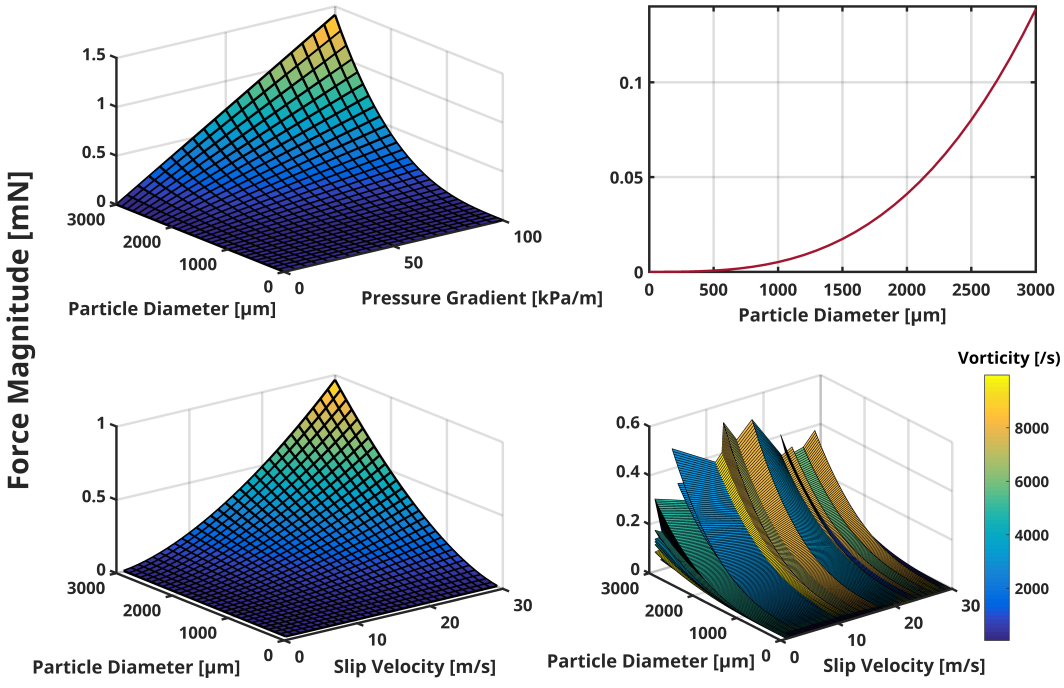

Figure 3.10: *Derived magnitude estimations based on the equations of Section 2.4, includes pressure gradient (TL), gravity (TR), drag (BL) and shear lift (BR).*

3.3.3 Integrity

It was also desired to investigate whether droplet distortion was relevant or if the integrity would always be maintained. Based on the We (Eq. (2.31)) and Oh (Eq. (2.32)), an analysis of the droplet integrity was conducted. Fig. 3.11 presents the relevant We of the system derived as functions of d_p and U_s, with the same ranges as Fig. 3.9, and Oh of the system as a function of d_p. This would find that $48 > We > 0$ was the maximum interval of the system. According to the literature presented in Section 2.5.1, droplet deformation and the multi-mode range of both bag-breakup and shear-stripping described in Section 2.5.2 could be significant. This indicated that distortion and breakup models should be included in simulations to adequately capture the droplet dynamics.

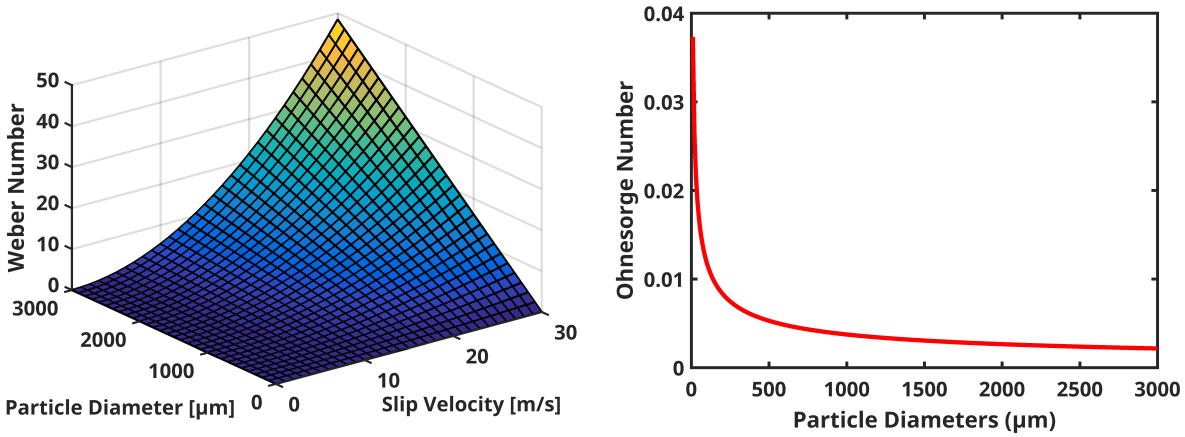

Figure 3.11: *Weber (L) and Ohnsorge (R) numbers of the system.*

3.3.4 Drag Coefficient Model

The derived We and Oh satisfies the validity range required to use Eq. (2.33). Thus, d_{def} could be derived together with the maximum increase in C_D due to deformation according to Eq. (2.20), as presented in the through the diameter ratio in Fig. 3.12. The plots show that the spherical assumption required for several of the forces in Eq. (2.14) will fail for larger droplets inside the wake where $U_s > 0$ due to inertia and subsequently $We > 1$ is expected. F_D in particular may differ significantly if deformations are excluded, thus the Liu-correlation (Eq. 2.20) was chosen over the Schiller-Neumann (Eq. 2.19) for computation of C_D.

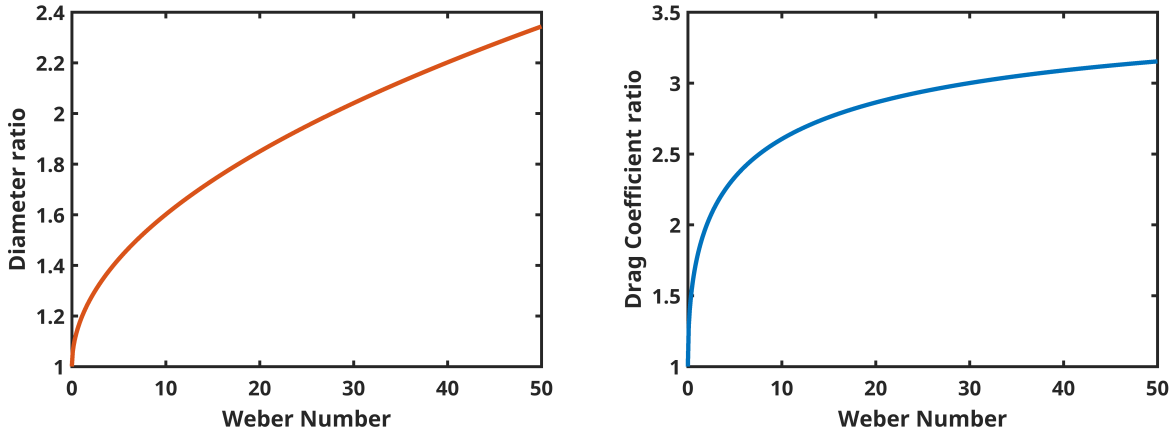

Figure 3.12: *Maximum possible diameter (L) and drag (R) ratios of the system as functions of the Weber number.*

3.4 Computational Model

With the finished geometries and selection of the droplet models, the computational model could be derived. The numerical method in its entirety is substantial and only the most significant details will be described to provide an adequate understanding of how simulations were setup.

3.4.1 Geometry preparation

The CAD models of the geometries would be discretized into a surface grid, serving as a basis for the discretization of the domain into the volume mesh.

3.4.1.1 Surface Mesh

The surface mesh was generated using quadratic cells of a 4 *mm* base size with edges and curved regions having some triangular cells of smaller sizes. The CMS was refined to adequately capture the curvatures of the CAD. In addition, the surface mesh of the CMS face was further refined through reduction of base size, growth rate and points per circle to increase the number of cells to roughly 15 000 for the surface contamination quantification method (Section 3.4.7).

The results of these refinements are presented in the Fig. 3.13 and would increase the resolution and accuracy of the surface grid, with the unrefined mesh hardly capturing any curvature. The exception would one region of the base where a deformation to the surface occurs as observed in Fig. 3.13. Finally, roughly 60 000 surface cells would be obtained through these methods.

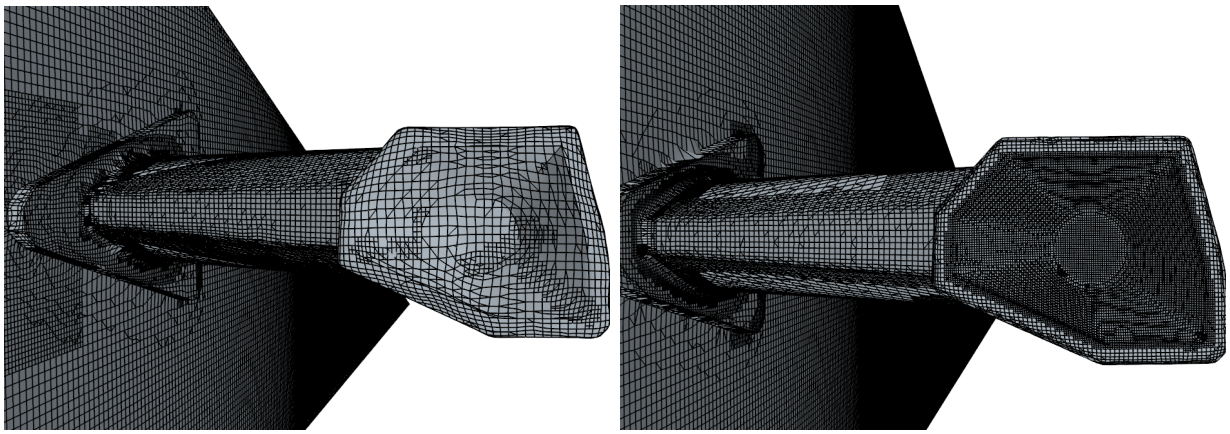

Figure 3.13: *Surface mesh of unrefined geometry (L) and refined CMS (R).*

3.4.1.2 Volume Mesh

Once the surface mesh was deemed sufficiently fine to capture the geometry, the volume mesh would be generated by growing cells from the surface grid. The growth rate from the base cubic cell size is exponential by multiples of 2, starting at a base size of 4 mm and increasing by

$$\Delta_i = 0.004 \times 2^i \Delta_0 \ , \tag{3.2}$$

for the ith level, with a base total of 8 levels were used for all simulations. Boundary regions would use a higher density of cells to allow for the all-y^+ treatment of the exterior surfaces of the geometry. The volume mesh and of the $70 \times 30 \times 40$ m Wedgeoid domain is presented in Fig. 3.14.

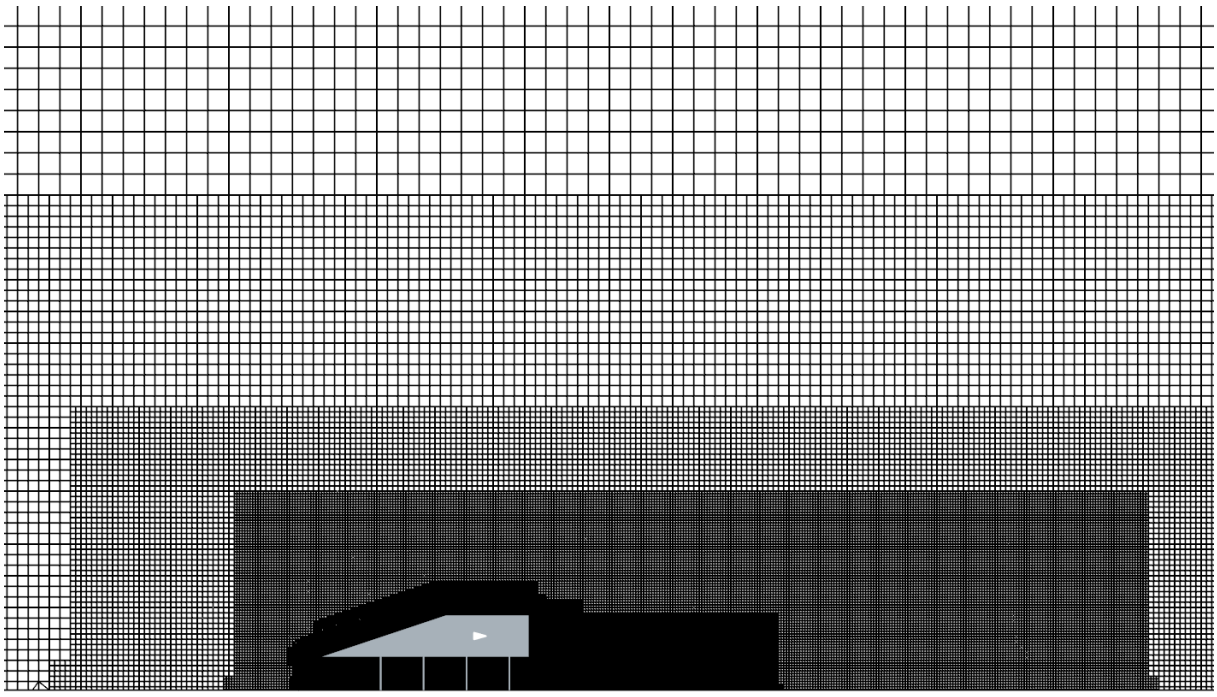

Figure 3.14: *Volume mesh of Wedgeoid, displaying several layers of the domain's volume mesh.*

Some refinements were deemed necessary to better capture the strong velocity gradients present at the CMS wake. Thus, an additional grid size level was added at the wake by projecting the face of the CMS arm, glareshield and lens through the use of wake refinements, presented in Fig. 3.15 where

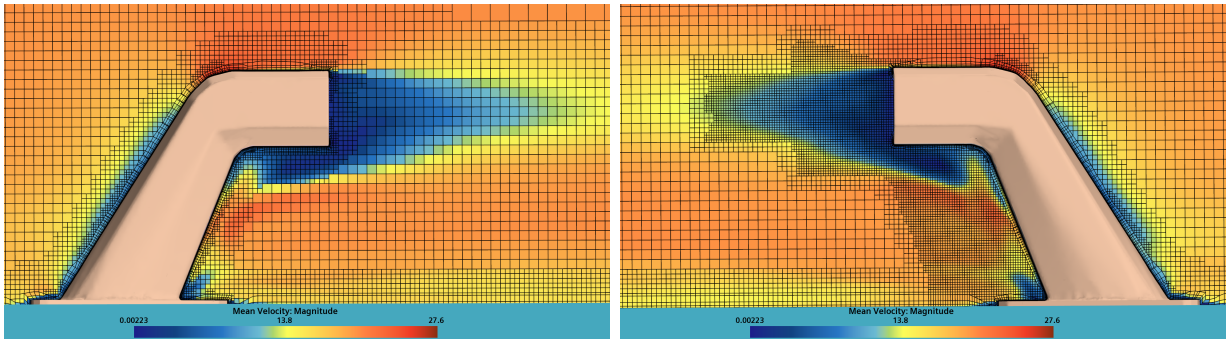

Figure 3.15: *Default volume mesh of CMS mean velocity (L) and wake refined counterpart (R).*

there a significant difference in the refined velocity field may be observed. The added resolution is not only beneficial for the smoothness of the gradients, but also for the amount of resolved turbulent kinetic energy, since DDES is the selected turbulence model which resolved turbulence down to the grid size, Section 2.3.1.3. This indicated that the refinement would increase the accuracy of the method.

Finally, roughly 26 000 000 volume cells would be produced through the meshing method.

3.4.2 Fluid Phase Models

The flow was assumed to be isotherm, incompressible and turbulent air with significant unsteady behaviour, with DDES as the employed as the turbulence model. The settings used in STAR-CCM+ are presented in Table 3.2.

Table 3.2: *Models of the air phase.*

Air flow Model	Setting
Time	Unsteady
Turbulence	$k - \epsilon$ DDES
Wall treatment	All-y^+
Multiphase	Lagrangian Particle Tracking

3.4.3 Droplet Phase Models

The Lagrangian framework was elected as a suitable approach for the one-way coupled droplets with all droplet phase models presented in Table .3.3. The included forces were chosen based on Fig. 3.10 and TAB distortion was included based on Fig. 3.11. Reitz-Diwakar Breakup was favored over TAB as breakup model due to the inclusion of modes

and the system's We being within the range of these modes. Fig. 3.12 indicated that the Liu-correlation should be used for C_D. Finally, as some the smallest volume cell size was 2 mm and it was believed that the smallest droplets would be affected by small scale turbulence, turbulent dispersion was included.

Table 3.3: *Final models of the droplet phase.*

Lagrangian Model	**Setting**
Particle type	Spherical Material Particles
Material	Liquid
Forces	F_D, F_g, F_L, F_P
C_D	Liu Coefficient
C_L	Summderfeldt Coefficient
Subgrid Drag	Turbulent Dispersion
Secondary Breakup	Reitz-Diwakar
Distortion	TAB

3.4.4 Boundary Models

Boundary models would be elected on basis of boundary type and are summarized in Table 3.4. The domain borders other than the inlet would be set to outlets. The inlet velocity would depends simulation, but would mostly be set to 70 km/h. The other boundary settings would remain constant over all simulations. All surfaces were treated as walls and blended wall functions were applied at the entire geometry exterior.

Table 3.4: *Boundary models and their settings.*

Boundary	**Model**	**Setting**
Inlet	Type	Velocity Inlet
	Direction	(1,0,0)
	Velocity	70, 90 or 120 km/h
	Turbulence specification	Turbulence Intensity + Viscosity Ratio
Outlet	Type	Pressure Outlet
	Pressure	0 Pa
	Backflow Specification	Environmental
	Turbulence Specification	Turbulence Intensity + Viscosity Ratio
Surfaces	Type	Wall
	Shear Stress Specification	No-slip
	Wall Surface Specification	Smooth
	Wall Treatment	Blended Wall Function

3.4.5 Solvers

Simulations were ran for 6.2 s in physical time, corresponding to several computational hours of roughly 44 000 iterations. By enforcing $CFL < 1$, droplets were permitted to

stay sufficiently long in each cell, as described in Section 2.2.1. The solver settings are presented in Table 3.5 with a more detailed convergence study presented in Appendix B.1.

Table 3.5: *Solver models and their settings.*

Injector Model	Setting
Temporal	Second Order
Spatial	Gauss-Seidel
CFL	0.05 - 0.35

3.4.6 Injectors

Two types of injectors were used in simulations, one emulating the primary road spray and one film ruptures presented in Fig. 1.3. Both set the droplets initial velocity to 0 and used a Rosin-Rammler size distribution for the particle diameters sampling but with different ranges.

3.4.6.1 Road Spray

The road spray injector was designed to emulate the tyre-stirred spray by a frontal vehicle travelling on a wet road and is presented in Fig. 3.16. It was modelled as point sources defined through a table consisting of roughly 40 000 points, positioned in a one-layer rectangular sheet 1.5 m away from the nose of the bluff body. The sheet had a height of 1 m and width of 2.2 m.

Table 3.6 presents the injector settings where the size distribution was based on research made on road spray generated by trucks [26], although the lower boundary was instead set to 1 μm to examine if these sizes would be sucked into the CMS wake.

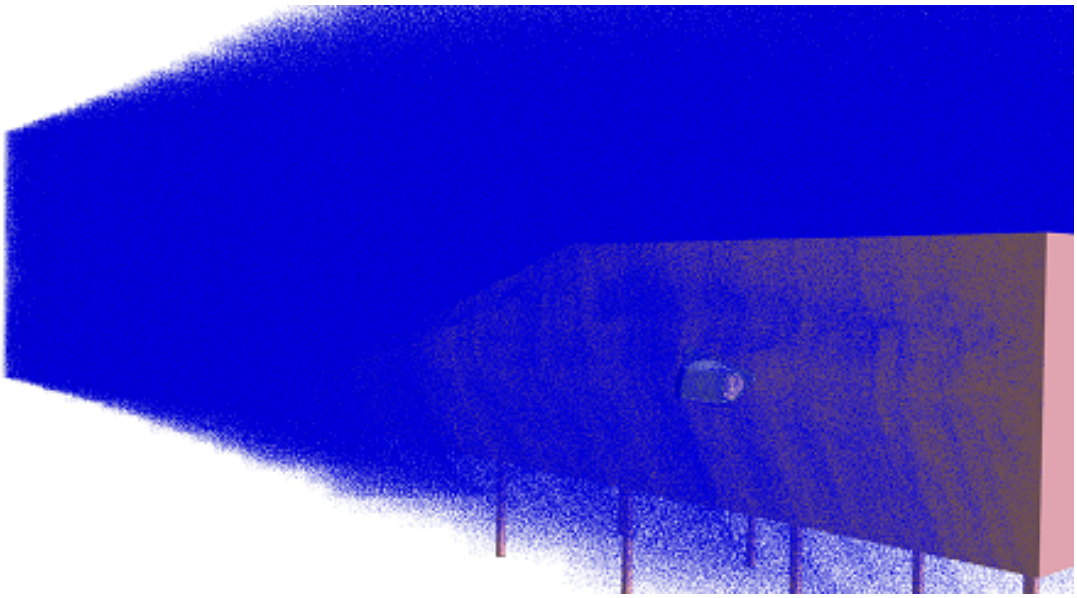

Figure 3.16: *Visualization of road spray injector spraying water droplets on wedgeoid geometry.*

Table 3.6: *Settings of road spray injector.*

Injector Model	Setting
Type	Table Injector
Particle Flow Rate	1 /s
Initial Velocity	(0,0,0) m/s
Particle Diameters	1-150 μm

3.4.6.2 Film Rupture - Circumference

The film ruptures originate from accumulated grounded droplets at the circumference of the CMS face for the groove-less designs. Since no film dynamics of deposited droplets was simulated, the approach was to attempt to emulate the ruptures by injecting droplets where they were expected to become airborne, at the circumference as presented in Fig. 3.17. In total, roughly 1500 injection points would be used and implemented in STAR-CCM+ as arbitrary probes of a surface with the corresponding settings presented in Table 3.7. The number of injector points and their density were meant as an extreme case to produce deterministic results that wouldn't be coincidental.

The method would however also inhabit several flaws, one being that the CMS designs that increase the circumference would have a lower injector points density. This was the case for the Enlarged GS and Slanted GS designs. Nevertheless, it was believed that this would coincide with reality if the CMS was subjugated to such extreme spray conditions.

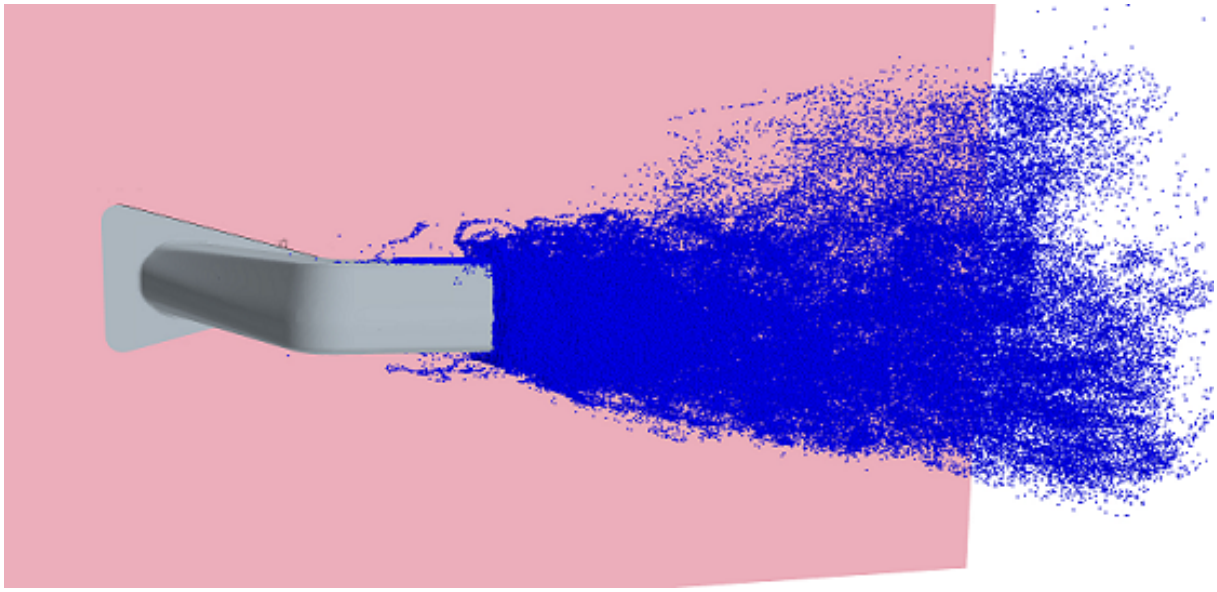

Figure 3.17: *Configuration of circumference film rupture injector emulating the secondary spray at the CMS edges.*

Table 3.7: *Settings of film rupture injector.*

Injector Model	Setting
Type	Table Injector
Particle Flow Rate	1 /s
Initial Velocity	(0,0,0) m/s
Particle Diameters	10-3000 μm

3.4.6.3 Film Rupture - The Ideal Groove

As for the groove family designs, the purpose of a groove was to lead away the migrating droplets from accumulating near the camera face. In the ideal case, all droplet would be released into the air away from the wake, at the patch underneath the CMS inside the groove ditch as is presented in Fig. 3.18. Thus, all injection points were placed at this location. This is the concept of the ideal groove which was deemed to be the appropriate film rupture injection configuration for the groove family. Finally, despite the possibility of larger droplets being released, the injector settings of Table 3.7 were used.

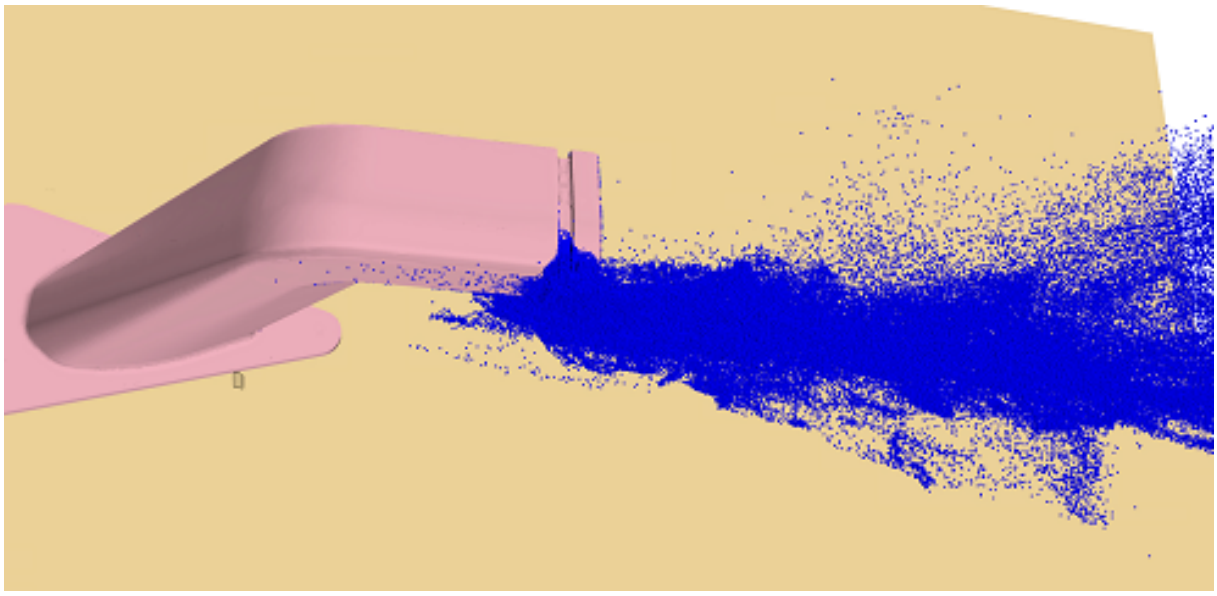

Figure 3.18: *Configuration of the ideal groove film rupture injector emulating the secondary spray at the bottom groove ditch.*

3.4.7 Contamination Quantification

By monitoring the mass of droplets in contact with the CMS lens and glareshield in STAR-CCM+, a useful quantity of contamination could be obtained. Since the model assumed that all droplets that collide with an exterior adheres, the mass of collided droplets would provide the total water that has soiled the region of interest if these are isolated.

However, since smaller droplets have significantly lower masses, scaling with d_p^3 if spherical, the total mass does not directly indicate how many droplets have soiled the CMS

or the coverage density. A field function in STAR-CCM+ was derived to estimate the surface coverage through number of contaminated cells by

$$\text{Contamination Criteria} = \left\{ \begin{array}{ll} 1 & if \quad \dot{m}_{p,cell} > 0 \\ 0 & else \end{array} \right\} , \tag{3.3}$$

which would summarize the surface of all contaminated cells and divide it by the total surface of the face

$$\text{Surface Coverage} = \frac{\text{Surface of Contaminated Cells}}{\text{Total Surface}} . \tag{3.4}$$

By monitoring both the colliding m_p and Eq. (3.3), contamination over time could be obtained.

3.4.8 Preformed Simulations

With all perquisites of the method satisfied, the simulations presented in Table 3.8 were conducted. Each simulation had two CMS prototypes attached to the lateral sides of the Wedgeoid, with the driver's side being equipped with the design of interest and the other side being equipped with a baseline for reference.

Table 3.8: *Preformed simulations, basic conditions indicate 70 km/h with default injector and physics settings.*

Simulation	CMS	Condition	Injectors
1	Baseline	Basic	Film Rupture and Road Spray
2	Baseline	90 km/h	Film Rupture
3	Baseline	120 km/h	Film Rupture and Road Spray
4	Baseline	Small Droplets	Film Rupture
5	Baseline	Schiller-Neumann C_D	Film Rupture
6	Deeper GS	Basic	Film Rupture and Road Spray
7	Enlarged GS	Basic	Film Rupture
8	Slanted GS	Basic	Film Rupture
9	Basic Groove	Basic	Ideal Groove Film Rupture
10	Slanted Groove	Basic	Ideal Groove Film Rupture
11	Aerodynamic Arm	Basic	Film Rupture

4

Results and Analysis

In this chapter, a selection of the obtained results will be presented and interpreted. The chapter is divided into a description of the simulated CMS flow field, an analysis of the general droplet dynamics in the CMS wake region and a presentation of the CMS designs' performance. The designs will evaluated both through simulation and experimental results.

4.1 The Region of Interest

The dynamics analysis of the later sections will be focused on the CMS wake region which is presented in Fig. 4.1 where there several significant features may be observed such as the size and shape of the CMS wake,

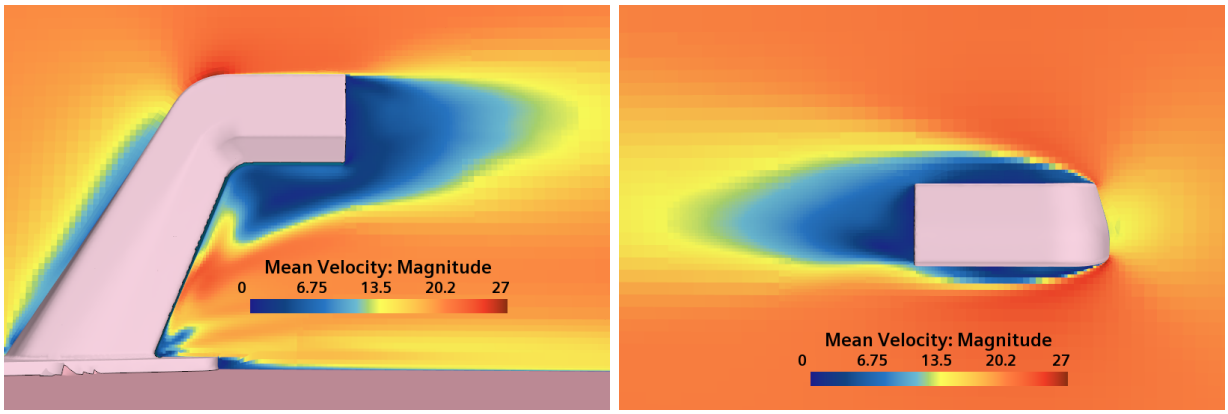

Figure 4.1: *Horizontal (L) and vertical (R) views of the mean velocity magnitude field of the baseline CMS attached to the Wedgeoid geometry.*

which is the region of interest. The arm wake is rather adverse, possibly due to a vortex displacing the air (Fig. B.3). The boundary layers of the camera head doesn't appear to be symmetric, probably due to the sloped shape. The head's bottom layer is thinner with a short transition to the free stream flow, while the top layer is thicker and puts some distance between boundary and free-stream. The top layer also merges with the wake, while the bottom layer seems to taper at the edge of the face.

Several other fluid properties are useful for the analysis of the results presented in this chapter, for more details of the aerodynamics of the baseline CMS, please see Appendix B.2.

4.2 Airborne Droplet Dynamics

In Section 3.3, physical models for the droplets' equation of motion was proposed, which in this section will be evaluated. Only the airborne droplets are of interest, as the Lagrangian model used fails for deposited droplets. In addition, only droplets in the CMS region are considered significant as properties of the flow are adverse here. All data is obtained at the simulations' final time-step, meaning that there is an excluded time dependence that could have impact the data.

4.2.1 Inertia

Fig. 4.2 presents Re_p and U_s obtained from simulating CMS contamination. As stated in Section 3.3.1, the time-insensitive inertia is difficult to quantify using Stk, as most of the droplets were expected to have $Re_p >> 1$ which is confirmed by the figure. Instead, a time-sensitive approach was to examine U_s as a function of d_p as this indicated how much they deviated from the flow at one point in time in the CMS wake region where strong velocity gradients were expected.

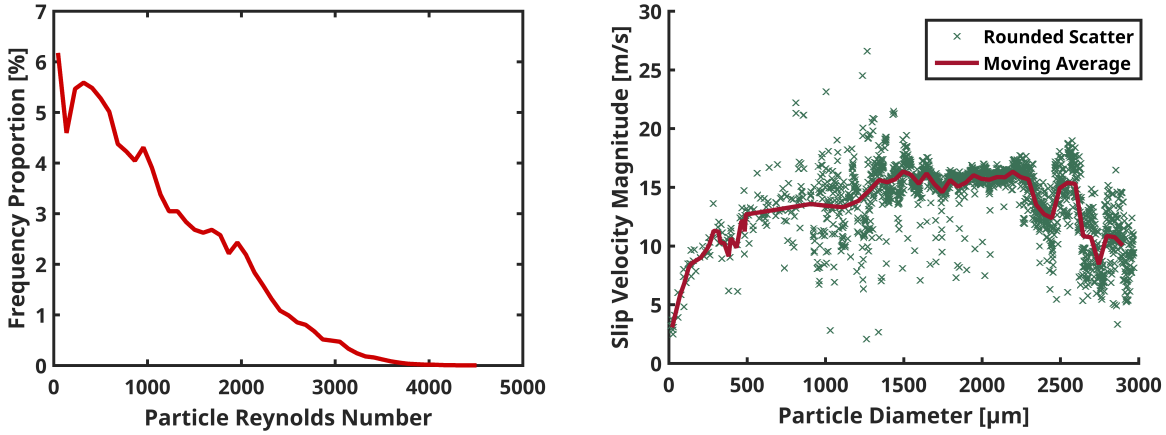

Figure 4.2: *Frequency of Reynolds particle numbers (L) and scatter of the droplets' slip velocities with their diameters and a moving average (R).*

The high proportion of droplets with $Re_p >> 1$ will have an impact on C_D and C_L (see Section 2.15). As for U_s, until $d_p \approx 2000\ \mu m$, the relation between the two properties seem to be that larger droplet respond slower to the flow, as expected. After this limit however, the droplets appear to be more responsive, something that will be discussed in Section 5.1.

4.2.1.1 Droplet Entrapment

It was also proposed in Section 3.3.1 that the droplets stirred up by frontal road sprays would only be entrapped within the CMS wake if $d_p < 20\ \mu m$. Fig. 4.3 examines this assessment by presenting the size of all droplets originating from the road spray injector (Fig. 3.16) that deposited on the baseline CMS face.

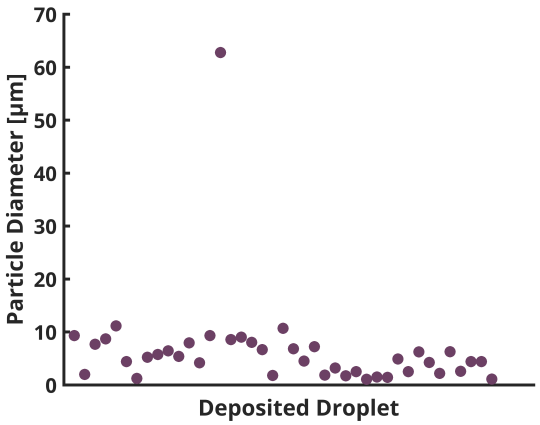

Figure 4.3: *Size of 40 deposited droplets originating from the primary road spray.*

The figure indicates that the theoretical critical d_p for entrapment is too large, as the limit seems to be $d_p \approx 10\ \mu m$, possibly due to either an incorrect τ_f or simply that Stoke's law is invalid due to most $Re_p > 1$. However, the theoretical limit was computed for $Stk = 1$ which is a limit of when $\tau_p < \tau_f$ that estimates when droplets will be responsive, not when they are completely carried by the flow. Thus, the limit of contamination may be $d_p < 10\ \mu m$, while the limit of responsiveness is $d_p < 20\ \mu m$. It should be noted that the lower limit of road spray droplets is in fact $d_p = 15\ \mu m$ and not $d_p = 1\ \mu m$ as used in simulations. Thus, it may be that no free-stream droplets reach the CMS face.

4.2.2 Integrity

To examine the possibilities of deformation and breakup, the distribution of We and y_{TAB} are of interest. Fig. 4.4 presents the frequency of default STAR-CCM+'s field functions of these quantities, both which indicate that a significant proportion of the droplets deform. It should be noted that the TAB plots used a 0.05 limit to indicate deformation proportion as all droplets are shown as if they have $|y_{TAB}| > 0$ due to the number of extracted bins and the bin covering the range near 0 having that limit.

Both ways of examining deformation indicate similar proportions of droplet that deform, which overall suggests that omitting the TAB distortion model would results in incorrect droplet sizes.

As for breakup, there is a relevant proportion of droplets within the range of bag-breakup that is used by the selected Reitz-Diwakar model. A similar proportion is also found in the TAB model, indicating both models being agreement on the proportion of breakup.

This is expected as both models use We for computation, but overall these plots confirms the necessity of the distortion models.

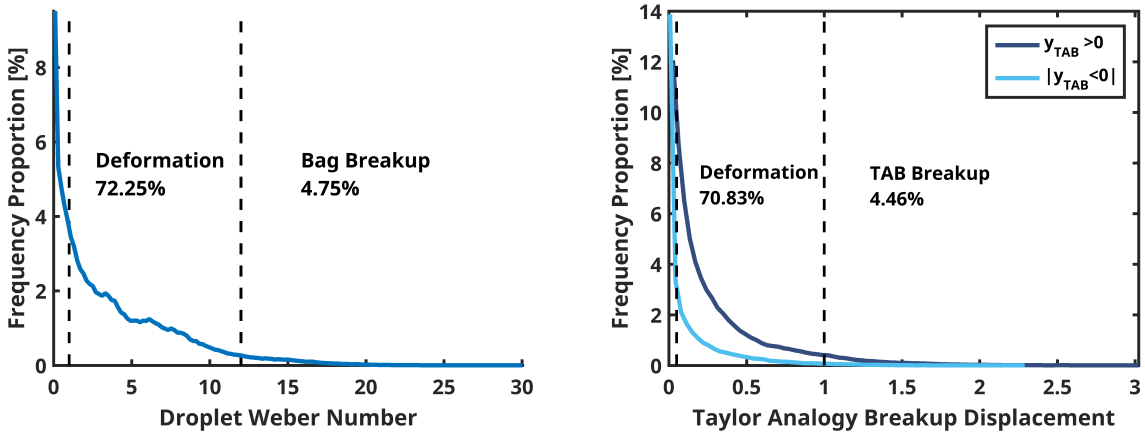

Figure 4.4: *Frequency of Weber numbers (L) and absolute values of TAB displacements (R) with proportions exceeding limit of deformation and breakup for respective model.*

4.2.3 Forces

Fig. 3.10 suggested the inclusion of F_D, F_P, F_g and F_L, a choice which now will be evaluated. Due to the great difference in order of magnitude of some droplet diameters, this evaluation will view small droplets ($d_p < 150\ \mu m$) separately for higher resolution. Fig. 4.5 presents the estimated forces for droplets of all sizes while Fig. 4.6 the corresponding estimations for the small droplets.

Comparing Fig. 4.5 to Fig. 3.10, F_D is as predicted the dominating force of the system. F_L appears to be considerably smaller than predicted, while F_P sizes up to F_D for the largest droplets. In comparison, Fig. 4.6 indicate that F_D completely dominates by an order of 1000 over F_P and F_L for small droplets, suggesting that both may be neglected. F_D now exceeds F_g by an order of 100, but given that F_g is always present it should probably still be included. See Section 5.1.2 for further discussion of the choice of forces.

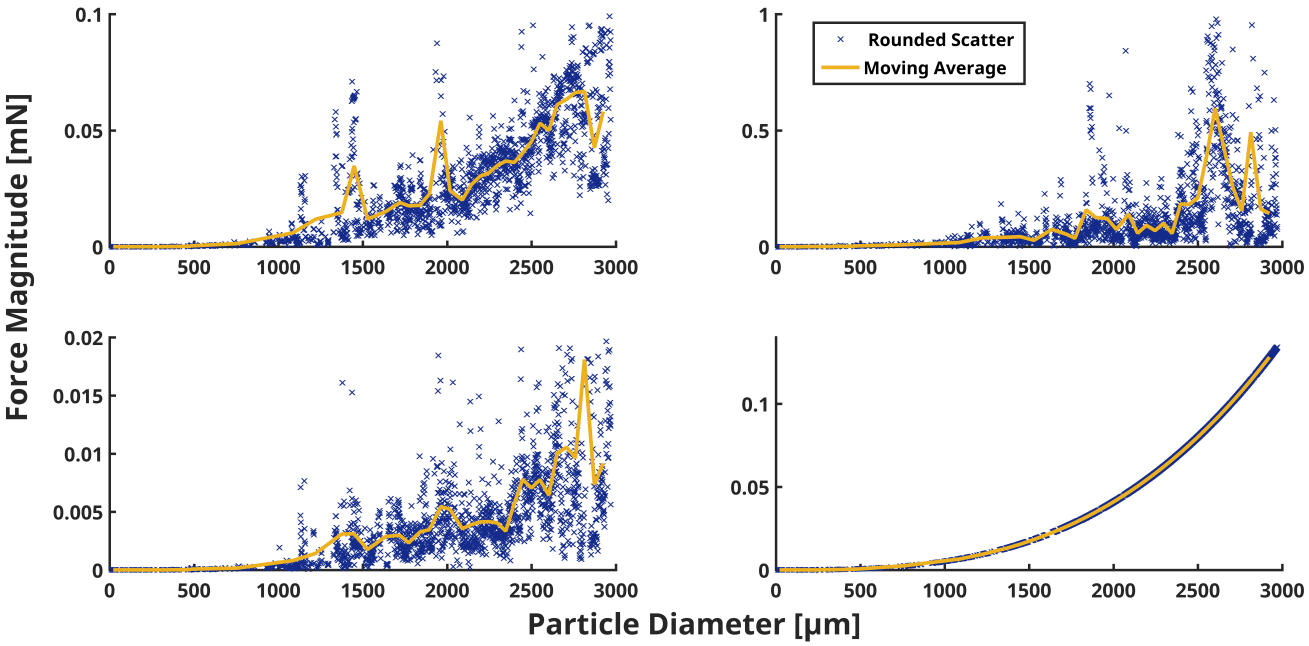

Figure 4.5: *Rounded scatter and moving average estimations of droplet force magnitudes in the CMS wake region of all droplet sizes. Includes drag (TR), pressure (TL), shear lift (BL) and gravity (BR).*

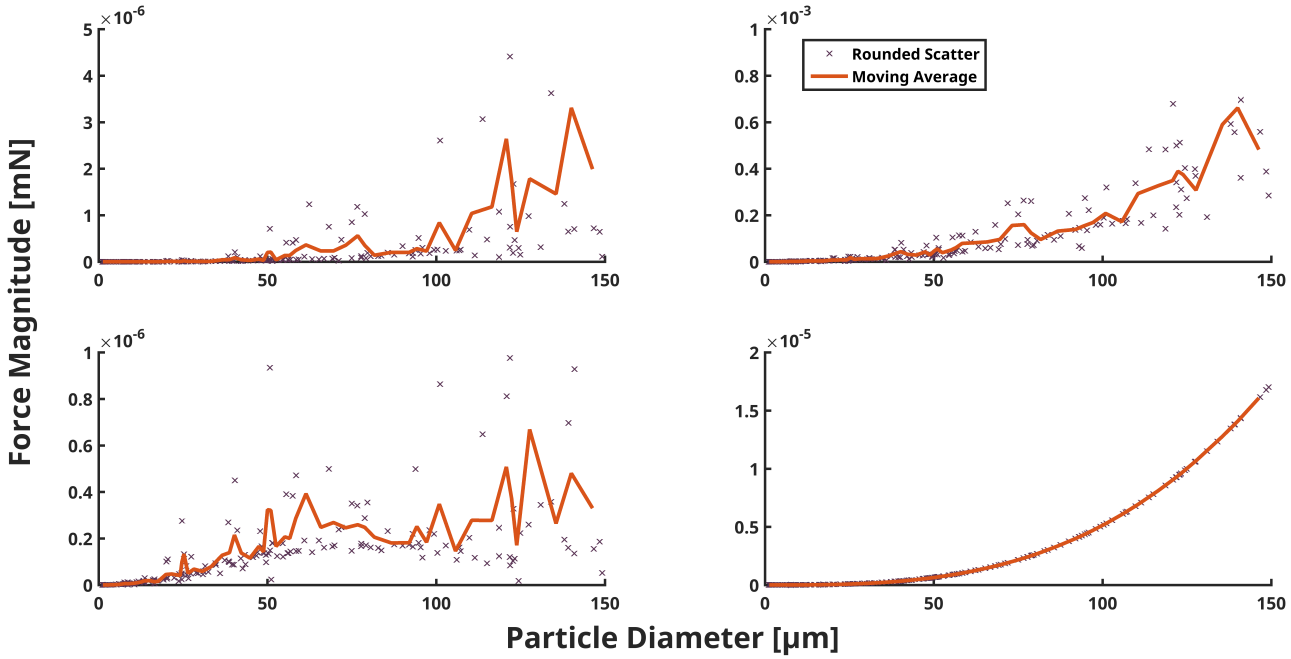

Figure 4.6: *Rounded scatter and moving average estimations of droplet force magnitudes in the CMS wake region, focused on the smaller droplets. Includes drag (TR), pressure (TL), shear lift (BL) and gravity (BR).*

4.2.3.1 Drag Model

It was hypothesised that the Liu-correlation was more suited than the Schiller Neumann due to significant droplet deformation, as was shown to be significant in Fig. 4.4. To examine how the model choice would impact C_D and F_D, the frequency distributions of F_D using either model's C_D was produced. In addition, the frequency distribution of the C_D-ratio between models was calculated and are presented in the Fig. 4.7.

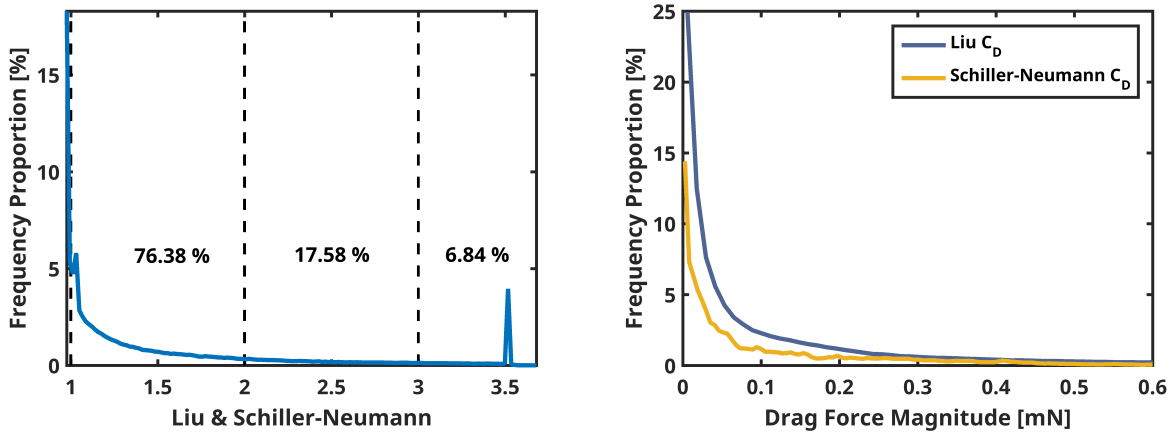

Figure 4.7: *Comparison of Schiller Neumann and Liu C_D models by ratio frequency distribution with marked limits of proportion exceeding ratio of 1,2 and 3 (L) and drag force (R) frequency distributions.*

The figure suggests that the majority of droplets have a higher C_D when using the Liu model, something which produces a systematic F_D difference. Note that the proportion that is < 1 in the ratio plot originates from the definition of the viscous regimes in STAR-CCM+ for each model, which differ only due to Liu using rounded values.

4.3 CMS Contamination - Simulations

In this section, the simulation results of CMS contamination of different camera designs and driving conditions will be presented. The different mechanisms of contamination will be evaluated, as will the droplet size distributions of deposited droplets.

In particular, the baseline CMS will be focused upon. The general contamination of the baseline in 70 km/h is presented in Fig. 4.8, visualized as a 2D-projection of droplets deposited on the CMS face with three marked regions that all display different contamination characteristics. The lens is less soiled, both in terms of size and number of droplets, with an overall lower deposition density. The outer GS is soiled by the majority of droplets. The largest droplets ($d_p > 2000\ \mu m$) are only found in the outer GS region, a satisfactory result as these contribute most to the absolute soiling. In conclusion, the baseline CMS lens is to an extent protected by the GS.

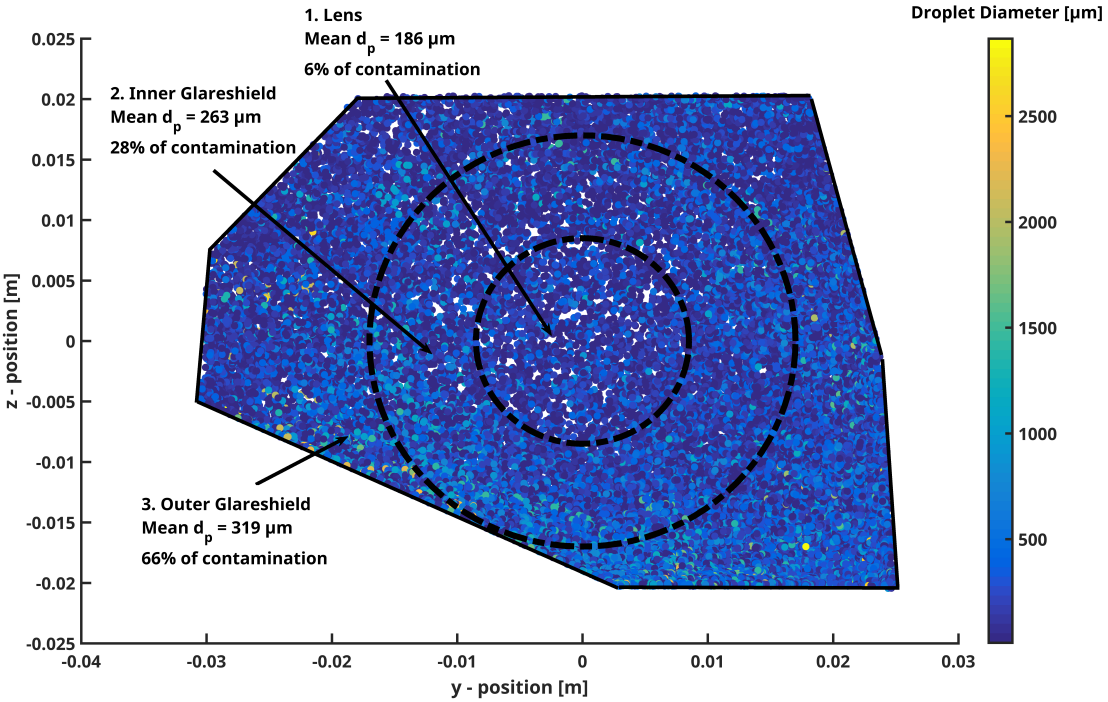

Figure 4.8: *Projection of soiling of the baseline CMS face in vertical direction, with droplet position given by (y,z)-coordinates an droplet size by colorbar. Three regions of the face are marked together with their corresponding mean deposited droplet diameter and deposition percentage of roughly 40 000 deposited droplets.*

4.3.1 Mechanisms

In Section 3.4.6 the two main injectors were defined as road spray and film rupture, but in Section 4.2.1.1 it was suggested that very few droplets from the primary road spray will reach the CMS face. Fig. 4.9 presents the coverage percentage and total mass of deposited droplets were monitored for the baseline CMS face, confirming the assessment that film rupture dominates.

Road spray does not contribute significantly to contamination, based on the $\sim$ 4.5 million droplets originating from the film rupture injector and $\sim$ 22 million originating from the road spray injector in Fig. 4.9. However, the difference in the injection density between injectors may cause the film rupture to inject far more droplets than in reality relative the road spray.

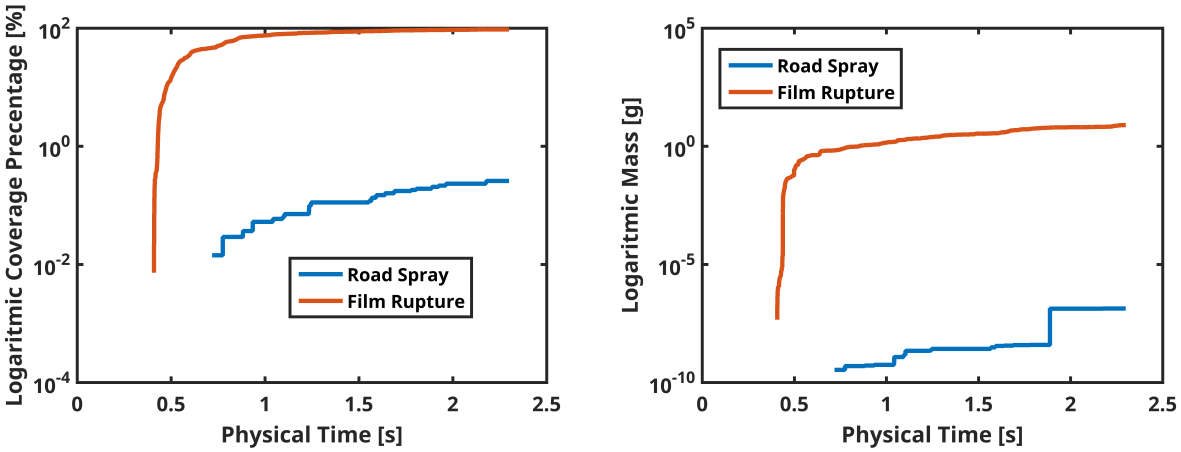

Figure 4.9: *Logarithmic coverage percentage (L) and total mass (R) of baseline CMS from road spray and film rupture droplets.*

4.3.2 CMS Designs

With the assessment that the film rupture mechanism completely dominates simulated contamination, the various CMS designs were evaluated based only on that injector. The contamination of all CMS designs was simulated and is presented in Fig. 4.10 where the results indicate that most added features to the baseline reduces contamination, with the exception of the slanted face feature.

Furthermore, to examine if the deposited droplet sizes changes with design, the size frequency distribution of deposited droplets on the CMS designs' faces were compared to the injected populations distribution, as presented in Fig. 4.11. The general trend appears to be that smaller droplet contribute most to contamination, probably a virtue of being more responsive to the chaotic trajectories of the wake and dominated by F_D. All changes in GS shape appears to permit larger droplets to soil the CMS face, with the Slanted GS design being most susceptible to large droplets. The faces of the groove family designs seems to be protected from all droplets larger than $d_p > 250\ \mu m$. For further comparison of designs, see Section 5.2.

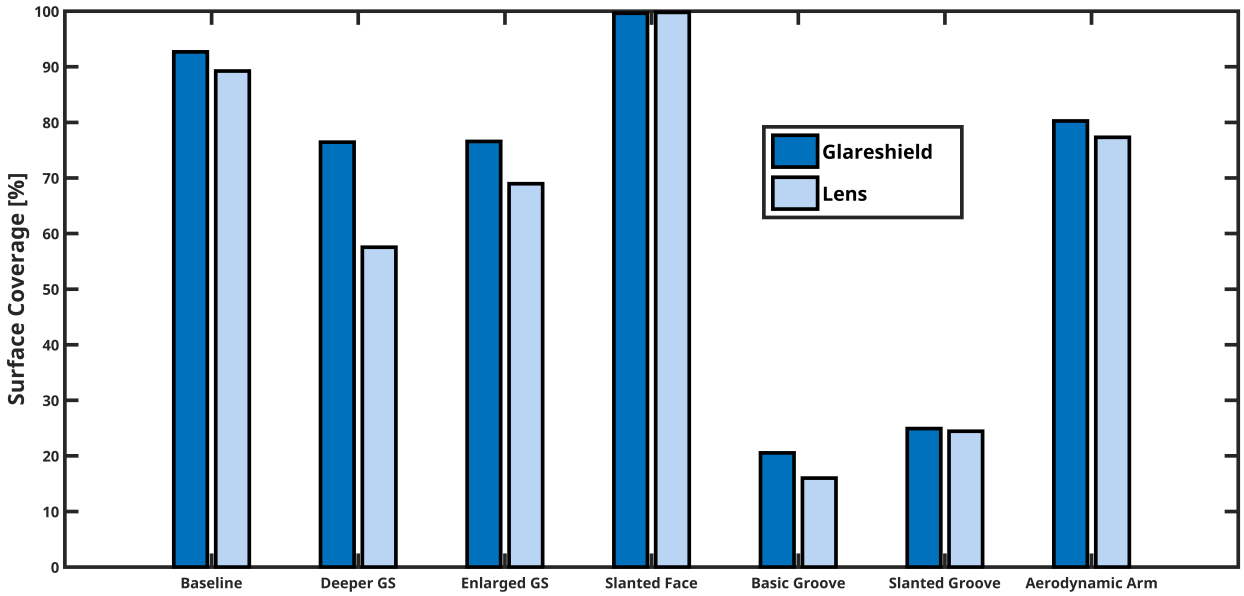

Figure 4.10: *Simulated covered CMS glareshield and lens percentages by water droplets of all CMS designs in 70 km/h.*

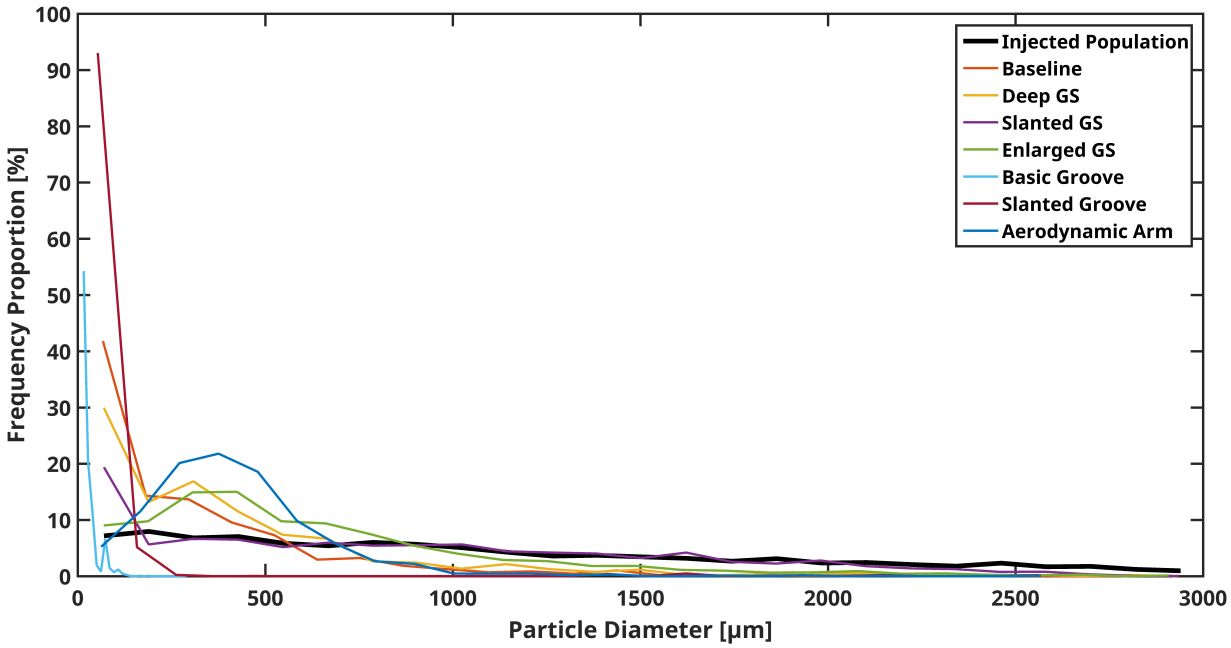

Figure 4.11: *Populations of deposited droplets on various CMS design faces, compared to the total injected population.*

4.3.3 Driving Conditions

Fig. 4.12 presents a comparison of contamination of the baseline CMS in three velocities. The coverage percentages aren't significantly distinguishable, as the variations are within the sensitivity marginal (Fig. B.8), which at the first glance would indicate that the film rupture of the simulations are velocity-independent.

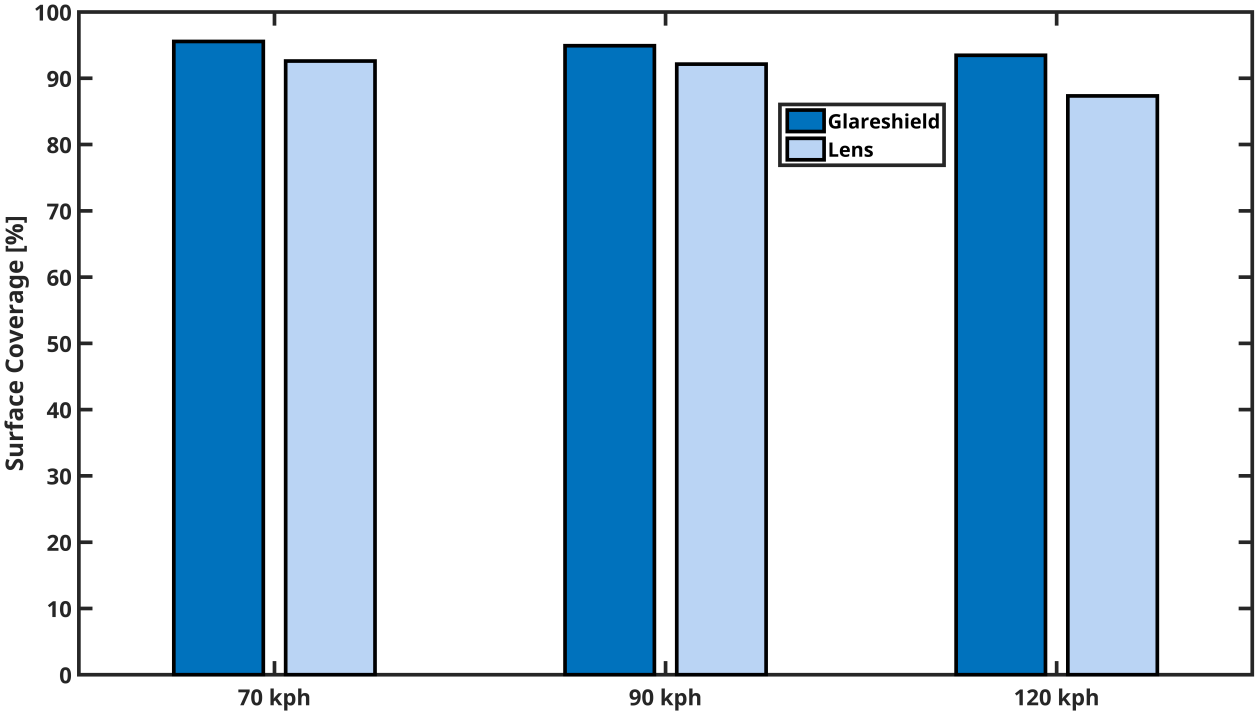

Figure 4.12: *Simulated covered surface percentages of baseline CMS by water droplets in different driving velocities.*

However, it is still possible that deposited droplet size relate to the driving velocity. Fig. 4.13 presents the frequency distribution of deposited droplet diameters and the monitored deposited water mass for the three velocities. From the sizes and deposited mass, it does appear that higher air velocity allows for more droplets of larger diameters to reach the CMS face, possibly due to the increase in F_D as inquired from Fig. B.7. This would indicate that given the same injected populations, higher velocities will see more contamination as the larger droplets occupy more real space, which is not reflected in Fig. 4.12 as contamination is quantified through number of occupied surface cells.

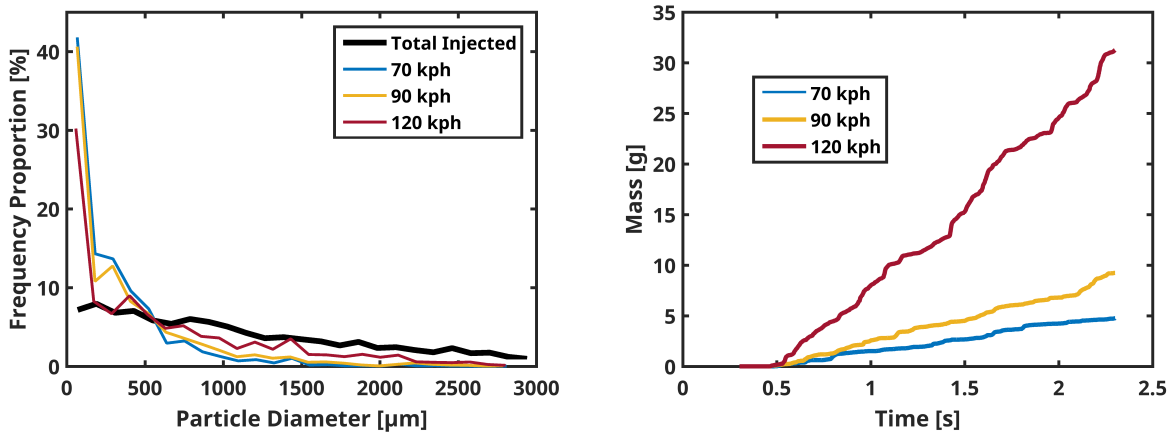

Figure 4.13: *Frequency distribution of droplet diameters (L) and mass of deposited water on CMS face (R) for simulations with different air velocity.*

Figure 4.14: *Rear and front view of final baseline CMS contamination by water droplets at 70 km/h, retrieved from the Wedgeoid experiment in the wind tunnel.*

4.4 CMS Contamination - Experiments

This section will present the experimental performance of all CMS designs and will focus on the baseline design in particular when evaluating mechanisms and driving conditions, where the general contamination of this design is presented in Fig. 4.14. Selections of recordings and snapshots will be used to illustrate mechanisms of contamination. The interpretations are made on observable droplets, meaning that the smallest droplets ($d_p < 200\ \mu m$, based on Fig. A.3) are excluded.

Fig. 4.14 shows how the face is soiled by a range of sizes, with accumulating films mainly at the bottom edges of the face. Unlike the simulations results of Fig. 4.8, the largest droplets seem to reach the lens region, however in the following section it will be proposed that these droplets does not originate from the film ruptures, but instead from grounded migrating droplets.

4.4.1 Mechanisms

It is the assessment that the road spray mechanism isn't significant, which is consistent with simulation results. The film rupture mechanisms appears to be significant, as also inquired from simulations. However, a second mechanism where droplet migrate onto the face from the exterior CMS surfaces was also observed and will be presented together with film ruptures in this section.

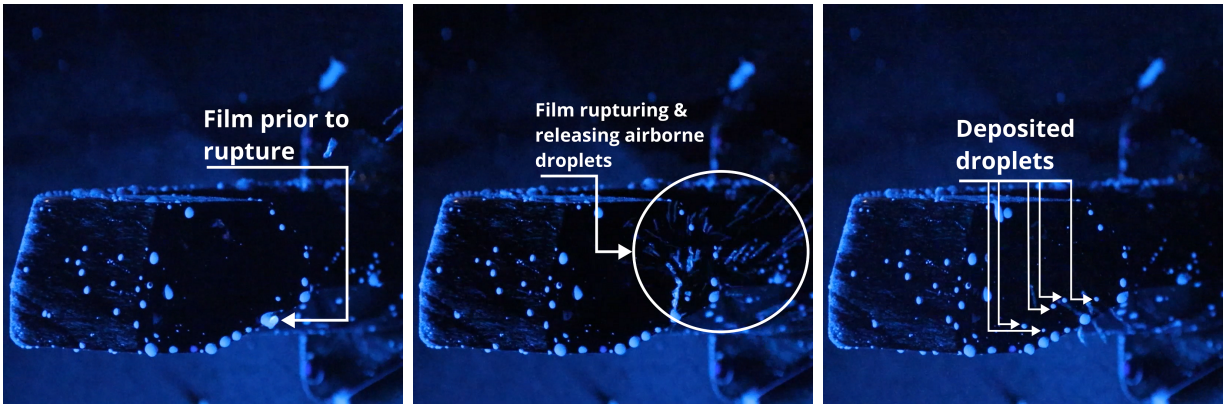

Figure 4.15: *Film reaching critical size and rupturing and releasing several droplets, some of which deposit on the CMS glareshield.*

4.4.1.1 Film Rupture

Fig. 4.15 presents an example of the physical film rupture mechanism. The observed mechanism is coherent with the literature and generally seems to contribute the greatest number of droplets to the contamination, of a wide size range which don't migrate or leave the face.

As may observed on the second frame of Fig. 4.15, a portion of the spray also travel downstream, possibly due to being outside the wake's reverse flow or inertia due to size, something that's consistent with simulations (Fig. 4.11). It would also appear that the larger range of film rupture droplets rarely reach the lens, which is also an observation made from simulations (Fig. 4.8).

4.4.1.2 Droplet Migration and Self Cleaning

Instead of rupturing, the film may instead migrate onto the CMS face and smear the surface, as is presented in Fig. 4.16. The droplet migrations contribute few droplets, around $10 - 20$ during a 5 minute trial, but these droplets may reach sizes of 5 mm (Fig. A.3). Thus, significance of the migration mechanism is comparable to film rupture.

The droplet migration phenomena can also remove other droplets, thus imposing a time-dependency on the results. This self-cleaning reduces the overall soiling and poses a significant challenge when evaluating experimental results through final contamination, since the face is decontaminated during the experiment. In simulations, where it is assumed

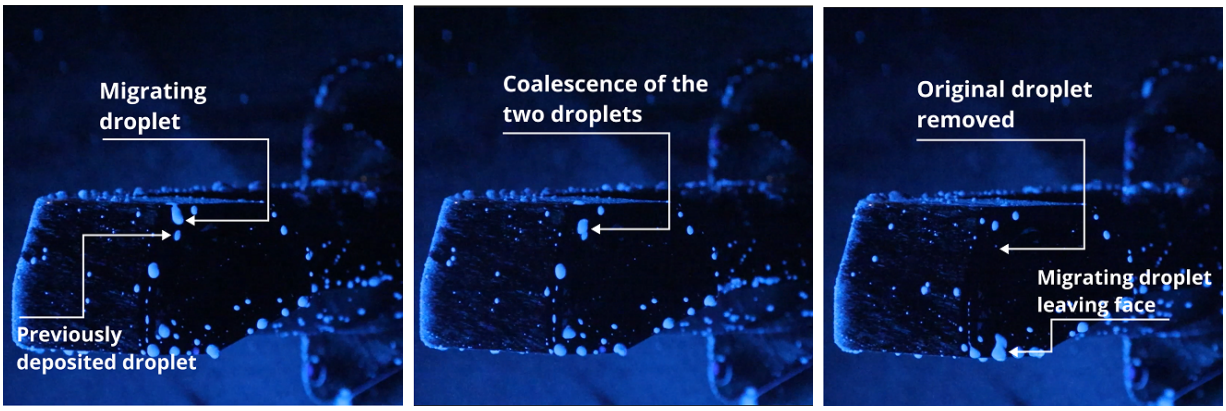

Figure 4.16: *Migrating droplet entering baseline CMS face from top, coalescing and removing a previously deposited droplet and eventually pouring of the face to be either released into the air or ruptured.*

that the accumulated films at the circumference of the CMS always rupture, droplet migration is completely excluded, as is the self-cleaning phenomena. This raises an inherent difference in experimental and simulation results.

4.4.1.3 Film Rupture - Real Groove

Generally speaking, film ruptures dominate at the bottom edges of the CMS face, whilst droplet migration is the more common mechanism at the top edge. The groove family members are an exception to this however, as droplets are prevented from reaching the top edge and instead accumulate on the bottom patch. However, in contrast to the concept of an ideal groove defined in Section 3.4.6.3, the groove doesn't rupture at the patch but rather overflows, still allowing for film ruptures at the bottom edge as illustrated in Fig. 4.17. Thus, the groove is not ideal but it does manage to prevent the largest droplets from migrating to the face. Whether this is desired or not depends on the effectiveness and consequences of the self-cleaning phenomena, a topic that is outside the scope of this project.

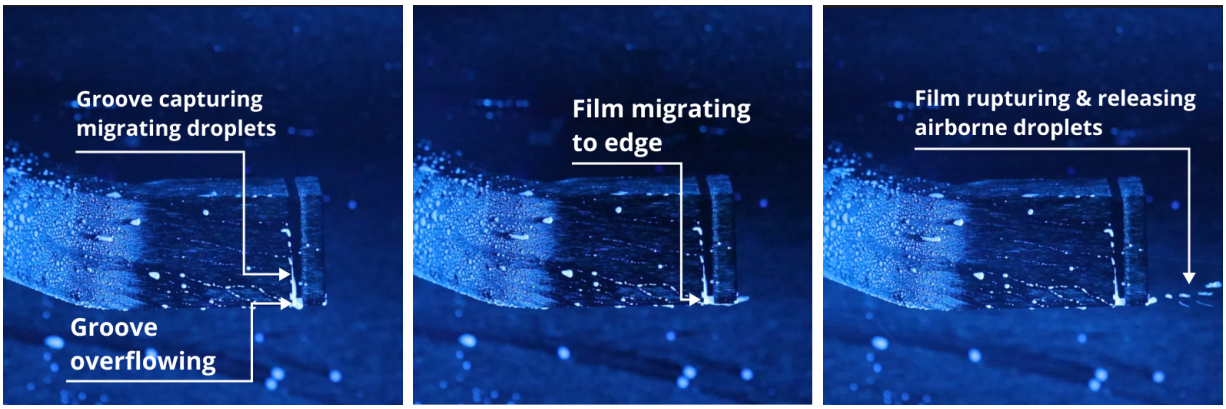

Figure 4.17: *Migrating droplets being captured by the groove and accumulated on the bottom patch until it overflows, allowing the film to migrate to the face's edge where it ruptures and releases airborne droplets.*

4.4.2 CMS Design

Despite the prominent droplet migration and self cleaning phenomena there was an attempt to present experimental soiling in a similar manner as the simulations (Fig. 4.10). The results of this are presented in Fig. 4.18 where the most notable difference to the corresponding simulation results in Fig. 4.10 is the general difference in coverage. Where most designs in simulations were around double digits, the experimental bars never exceed single digits. This may be due to the injector configuration and contamination quantification of the simulations, see the Chapter 5 for further discussion.

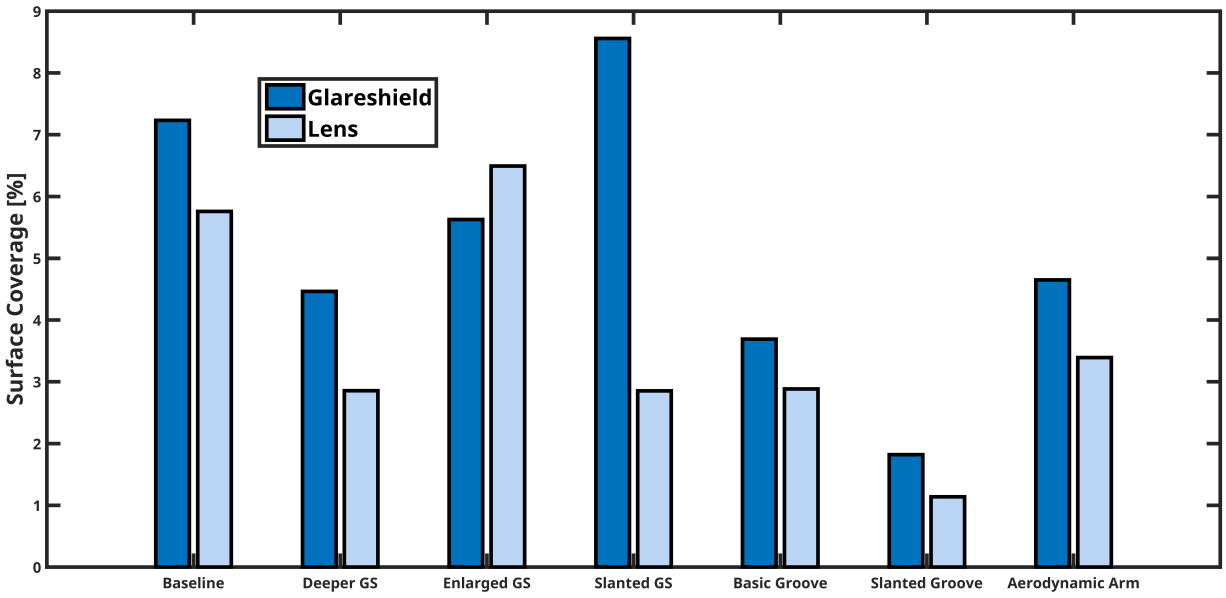

Figure 4.18: *Experimental Glareshield and lens droplet coverage by water droplets of all CMS designs in 70 km/h.*

Fig. 4.18 takes the surface coverage of the CMS designs at the end of a trial, thus they are time-insensitive. In contrast, Fig. 4.19 presents contamination of the baseline CMS in the wind tunnel over time. The data has been filtered to focus on systematic deviations from the mean which shows that the lens is much more sensitive than the glareshield and is poorly evaluated based on its final contamination. The glareshield however does show a consistent increase over time, indicating that its final coverage percentages in Fig. 4.18 may be representative. There is a difference in the measure coverage percentage compared to Fig. 4.18 due to different images from the same trial being used for computation of the contamination.

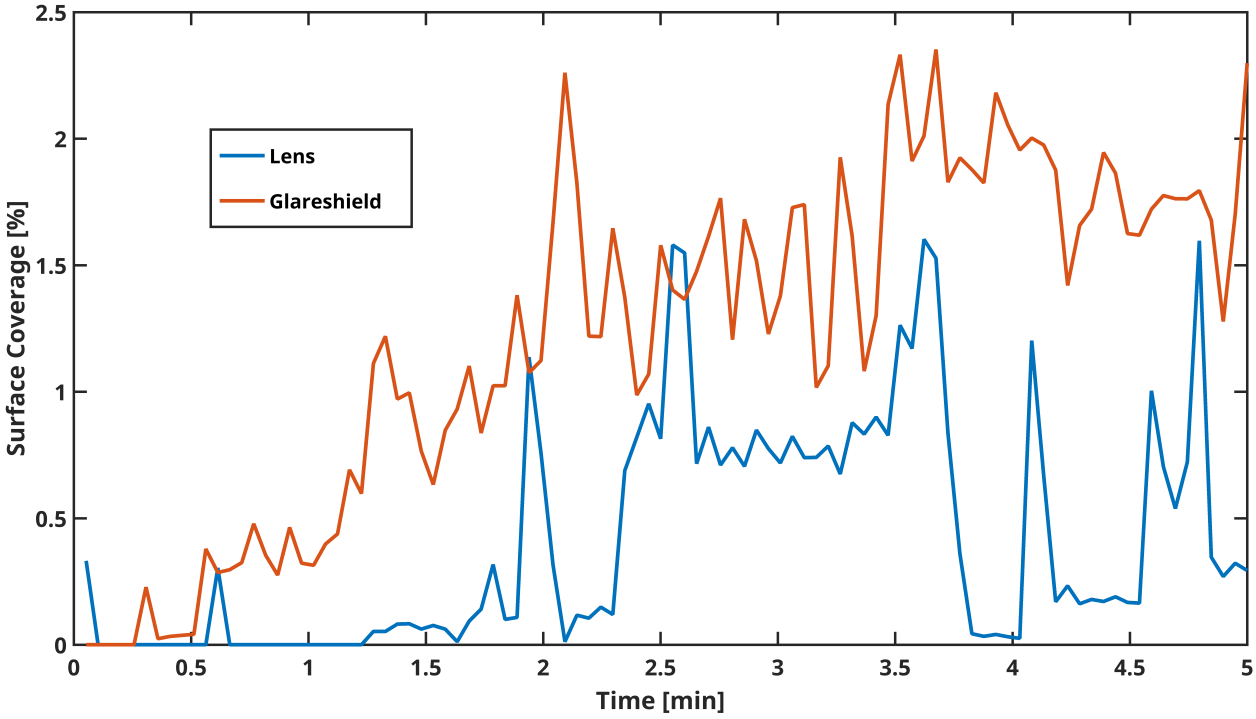

Figure 4.19: *Experimental glareshield and lens droplet coverage rates by water droplets of baseline design in 70 km/h.*

4.4.3 Driving Conditions

Similarly to simulations, the impact of different air velocities were evaluated and presented in Fig. 4.20. As with Fig. 4.18, the lens coverage display a high variation, whilst the GS coverage increases slightly with velocity. To say that it indicates a velocity dependence would be generous as there is most likely a variation between repetitions that exceeds the presented GS differences.

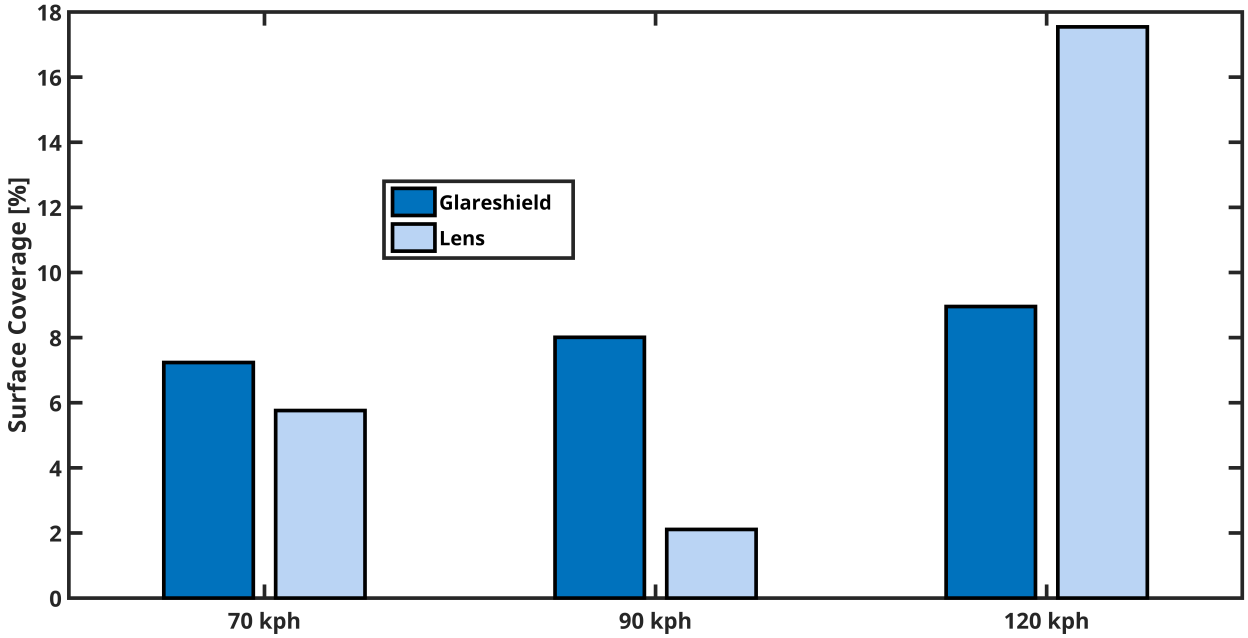

Figure 4.20: *Experimental Glareshield and lens droplet coverage by water droplets of baseline CMS in 70, 90 and 120 km/h.*

5

Discussion

In this chapter, the overall results will be discussed. In contrast to Chapter 4 where results were presented with some basic interpretations, this chapter will discuss the results in a both a broader and deeper sense to derive the final conclusions.

5.1 Droplet Physics Models

It was suggested in Section 4.2.2 that droplet distortion models should be included together with Liu's C_D. There were however some results that weren't as apparent and will therefore be discussed further in this section.

5.1.1 Droplet Responsiveness

In Section 4.2.1 it was shown that U_s levels off and even decreases after $d_p > 2000\ \mu m$. Based on figures 4.5 and 4.6, there is a possible explanation to this behaviour. Smaller droplets are completely dominated by F_D, but for larger droplets F_P will become significant and comparable to F_D as C_D decreases with Re_p until $Re_p > 1000$ where a constant $C_D = 0.44$ is obtained. Adding on to that, F_P increases with the cube of d_p while F_D increases only by the square. In fact, F_P seems to increase rapidly at $d_p > 2000\ \mu m$. This suggests that the U_s increases with d_p due to inertia as expected until $d_p \approx 2000\ \mu m$, at which U_s levels off as ∇P aligned with the direction of the flow counters the inertia and increases the responsiveness to the flow, causing U_s to decrease for the largest droplets.

5.1.2 Choice of Forces

The included forces have significance on results and computational efficiency. By omitting significant forces, the droplet's motion will be inaccurate and by adding every possible force the risk for model error increases, as does the solver time. Based on the results presented in Section 4.2.3, F_D should always be included and it could be argued that F_G should too on basis of consistently acting on droplets. It was also shown that Liu's C_D should be used for F_D (Fig. 4.7), but for C_L which is used for F_L no alternative models were found that considered deformation. It was suggested that F_L could probably be ignored, and given that the deformation is orthogonal to the flow direction, it will be parallel to F_L meaning that the droplet will appear compressed, thus reducing the magnitude of the force, further advocating for its neglection.

If film rupture droplet indeed reach sizes of 3 mm, F_P should be included, but at $d_p < 2\ mm$ it would appear to be unnecessary. It should be noted however that both of F_P and F_L do however depend on the geometry and it is possible that less aerodynamic features could make these forces more significant.

5.2 The Better CMS Design

One of the main aim of the project was to evaluate how the design features added to the baseline CMS affected soiling of the face. In this section, the different CMS designs will be evaluated using the simulation results (Fig. 4.10) and experiment results (Fig. 4.4.2)

5.2.1 Shape of the Glareshield

Overall, it would appear that only the Slanted GS design is more susceptible to soiling. The fact that the coverage $\rightarrow 100\%$ in simulations would indicate the possibility of even higher soiling, as the surface contamination quantification method require free surface cells that will eventually run out. This is further confirmed by Fig. B.6, where it may be observed that the surface coverage of the Slanted GS design converges as opposed to the baseline and 5 times the mass have been deposited on the slanted design. In experiments, this design would get the most soiled GS, which through Fig. 4.19 was deemed as representative.

The Enlarged GS design seems to be less soiled, perhaps due to a larger surface, although it should also have a larger wake which is probably why larger droplets soil it, compared to the baseline (Fig. 4.11). In particular, the lens is comparatively less contaminated in simulations, as is the case with the lens of the Deeper GS design. This would indicate that adding distance to the lens does reduce soiling as droplets have to travel farther to reach the it.

The lens coverages in experiments were unexpected, but Fig. 4.19 suggested an experimental the sensitivity of the lens to migrating droplets which would suggest that film ruptures aren't necessarily the largest issue and prompts the need of a groove.

5.2.2 Effectiveness of a Groove

The ideal groove does indeed avoid the majority of airborne droplet deposition by preventing film ruptures near the wake. However, the Slanted Groove design appears to be more contaminated in simulations despite its greater distance to the CMS face. The reason may be inquired from the flow field of Fig. 4.1 compared with Fig. 3.4 where it appears as if the Basic Groove sprays droplets into a thinner part of the boundary layer, allowing them to carried by the air current downstream, as opposed to the Slanted Groove design where droplets are released deeper into the boundary layer and run a higher risk of being carried to the wake as their momentum is lower. Fig. 4.11 adds to this hypothesis, as the Slanted Design permits larger droplets to reach the face, whilst for the Basic Groove, any droplet with significant mass will most likely exit the boundary layer due to F_g.

As for the experimental counterparts, both groove designs still preform better compared to the rest, however the relative difference is smaller compared to simulations. This may be explained by Section 4.4.1.3 displayed how the designed groove is not ideal as instead of rupturing at the bottom patch, the groove overflows and permits film ruptures into the wake. The real groove still preforms better than any other design, probably due to it preventing migrating droplets to enter the face which was shown in Section 4.4.1.3. The Slanted Groove is also less soiled than the Basic Groove in experiments, which could be due to the added distance for overflowing film fragments to migrate at the bottom surface of the CMS head.

5.2.3 Aerodynamic Arm

The design would appear to be less soiled than the baseline in both simulations and experiments. In appendix Fig. B.5, the flow field of this design is presented and it may be observed that the wake has been reduced in size compared to the baseline (Fig. 4.1). A smaller wake means a smaller volume that can entrap airborne droplets, which would explain the reduction. However, the deposited sizes of the Aerodynamic Arm design in Fig. 4.11 are adverse, as relative large droplets soil this design. This contradicts the previous statement, as a smaller wake should prevent larger droplets to be entrapped. This is an adversity of further investigation not presented in this project.

5.3 Driving Velocity

In simulations (Fig. 4.12) there is a relationship between deposited mass and air velocity that is not found in experiments (Fig. 4.20). The reason for this may be related to the droplet migration mechanism. In appendix Fig. B.9 a case of film rupture being favored over droplet migration is presented, despite being located at the top face edge. It may be that as the velocity increases, We of the film does too causing them to favor rupture at the edges, as is the surface tension of water that permits the droplet to enter the face. This could lead to the expected increase in soiling due to larger film rupture droplets at higher velocities being balanced by the reduction of the largest droplets from migrations.

5.4 Model Accuracy

An important matter to consider is the validity of the model, as there are limitations and other choices that together made it possible to obtain the results.

5.4.1 Computational Errors

CFD simulations have both numeric errors and modelling errors. The numeric errors arise from the discretization of the physical models and how the entities in each discrete element is computed, i.e the numerical schemes and solvers. The numerical error has not been evaluated other than the refinements presented in Section 3.4.1. The convergence analysis of Appendix B.1 examines some properties of the solution, which deemed it

adequate. Some physics models were evaluated in Section 4.2, while some where chosen based on assumptions and literature. For instance, F_{VM} was never properly estimated, thus it's true impact remains unknown.

5.4.2 Simulation and Reality

As stated in Section 4.4, the droplet migration mechanism was completely excluded from simulations, which caused an inherent difference. Nevertheless, it was the ambition of this project that the simulation results will increase the understanding of the contamination by the airborne droplets in particular. There is reason to believe that the model satisfies this, as when examining the deposition trends of the film rupture droplets both simulations (Fig. 4.8) and experiments (Fig. 4.14) both agree that the larger droplets tend to deposit on the outer GS which protects the lens. This indicates that the flow field and droplet physics are at least similar to reality, if the proposal of the largest droplets originating from migration is accepted.

However, one important similarity between simulations and experiments are that both cases present similar GS-coverage comparisons between designs. For instance, only the Slanted GS design exceeds the baseline in both cases. The high variety in lens coverage may be due to sensitivity of its small surface to the large migrating droplets as suggested in Fig. 4.19. The spikes in this figure shows that a migrating single droplet is enough to add several percentages to the lens contamination, whilst the GS with its larger surface is not as sensitive to this. Overall, due to the time dependency of migrating droplets, this figure does not provide the same accuracy as the simulation counterpart.

Furthermore, both simulations and experiments do appear to agree that the free stream droplets are expected to ignore the reverse flow of the wake and not serve as a significant source of airborne contamination droplets.

6

Conclusion

Comparison between theory and simulations suggested that free-stream droplets with $d_p > 20\ \mu m$ are likely to ignore the wake and few droplets within that limit will contaminate the CMS face, if such small droplets exist at all in road sprays. Droplet response to the the flow would decrease with increasing d_p until $d_p \approx 2$ mm where F_P would be large enough to counter their inertia.

The majority of the wake droplets are deformed by the aerodynamic inertia and a smaller portion may fragment into smaller droplets, if the upper droplet size limit is true. Furthermore, the results also suggested that the F_D would always be the dominating force, regardless of droplet size. It was shown that the omission of the droplet deformation would give rise to a systematic underestimation of F_D. It was also proposed that F_g should always be included, while F_P should only if droplets are larger than 1-2 mm.

As for CMS soiling, it would appear that the majority of airborne droplets that reach the baseline's face originate from film ruptures. It was shown that 94% of droplets would deposit on the glareshield which were larger ($< d_p >= 291\ \mu m$) than the 6 % that reached the lens ($< d_p >= 186\ \mu m$). However, at higher air velocities droplets sizes that contaminated the CMS face would increase.

The largest droplets (>3 mm) would originate from grounded migrations, some even reaching the lens causing its experimental results to be more time-sensitive than the glareshield's. This phenomena would be more prominent for CMS designs without a groove in lower air velocities. This mechanisms was however outside the scope of the project and not simulated.

In simulations, CMS designs that added distance to the lens would be less contaminated, while slanting the GS would make the lens more susceptible. In the case of the ideal groove, it would too help reduce soiling by leading away the rupture regions and only permitting the smallest droplets to reach the wake, a trend which was difficult to observe in reality as the groove would overflow. The real groove would still contribute to a reduction in soiling due to capturing migrating droplets. Finally, soiling would decrease when reducing the size of the CMS face wake.

7

Future Work

Combining the Lagrangian approach of the airborne droplet with for instance a liquid film or volume of fluid model would be one good way to include the droplet migration mechanism, which has been shown to very significant. It should be possible to develop a criteria for whether a accumulated film will rupture or migrate on to the face based on We. If too complicated, another development to the injectors would be to predict injection points based on the wall shear stress.

All droplet dynamics should be monitored in STAR-CCM+ to retrieve averages rather than time-specific values. It would also be useful to actually track the simulation break ups to quantify how many droplets are formed with break up models. It may be that the break-up models may be excluded on basis of airborne droplets being smaller than 3 mm or that they only form a negligible amount of fragments.

Producing contamination over time plots for all experiment cases would be one way to retrieve more representative data. This could be done with the existing videos taken from the experiments.

The true size distribution of film rupture droplets should be measured. Probably, their size will increase with velocity which should also be measured. Using true size distributions, the importance of F_P could be better evaluated. This should also be done for the overflowing real groove, as those film ruptures may produce larger droplets.

It should be possible to expand the simulation method of this project to include contamination by rainfall, without having to change much other than the free-stream droplet sizes.

Finally, a combination of the CMS designs should be tested. Preferably, a groove should always be used. This could be combined with the aerodynamic arm to reduce the CMS wake size. Enlarging the glareshield increases the size of the wake, which is not preferable. Thus, a deeper glareshield should be combined with the groove and aerodynamic arm to form the best CMS design.

Bibliography

[1] WHO, "Road traffic injuries," 2022. [Online]. Available: https://www.who.int/news-room/fact-sheets/detail/road-traffic-injuries.

[2] Arbetsmiljöverket, "Huvudsakliga risker i trafiken," 2022. [Online]. Available: https://www.av.se/halsa-och-sakerhet/sakerhet-i-trafiken/huvudsakliga-risker-i-trafiken/#.

[3] NHTSA, "Driver assistance technologies," 2020. [Online]. Available: https://www.nhtsa.gov/equipment/driver-assistance-technologies#collision-intervention-30656.

[4] "What is adas?" *Oxford Technical Solutions*, Nov. 2020. [Online]. Available: https://www.oxts.com/what-is-adas/.

[5] I. Isaksson-Hellman and M. Lindman, "Using insurance claims data to evaluate the collision-avoidance and crash-mitigating effects of collision warning and brake support combined with adaptive cruise control," in *2016 IEEE Intelligent Vehicles Symposium (IV)*, 2016, pp. 1173–1178.

[6] K. Kovacic, E. Ivanjko, and H. Gold, "Computer vision systems in road vehicles: A review," *CoRR*, vol. abs/1310.0315, 2013. arXiv: 1310.0315. [Online]. Available: http://arxiv.org/abs/1310.0315.

[7] F. Comunicacion, "Cms audi e-tron," *flickr*, Dec. 2018. [Online]. Available: https://www.flickr.com/photos/ficosaofficialpage/31467046787.

[8] F. Comunicacion, "Cms audi e-tron," *flickr*, Dec. 2018. [Online]. Available: https://www.flickr.com/photos/ficosaofficialpage/44589655990.

[9] N. H. T. S. A. G. H. S. B. Elizabeth N. Mazzae and T. R. C. I. Adam T. Andrella, "Examination of a prototype camera monitor system for light vehicle outside mirror replacement," in *U.S. Department of Transportation*, 2016.

[10] A. P. Gaylard, K. Kirwan, and D. A. Lockerby, "Surface contamination of cars: A review," *Proceedings of the Institution of Mechanical Engineers, Part D: Journal of Automobile Engineering*, vol. 231, no. 9, pp. 1160–1176, 2017. DOI: 10.1177/0954407017695141. eprint: https://doi.org/10.1177/0954407017695141. [Online]. Available: https://doi.org/10.1177/0954407017695141.

[11] D. Tsepov, N. Solomatin, A. Zotov, and D. Rastorguev, "Formation analysis of soiling for side windows and the rear view mirrors of vehicle," *IOP Conference Series: Materials Science and Engineering*, vol. 632, p. 012 068, Nov. 2019. DOI: 10.1088/1757-899X/632/1/012068.

[12] T. Eidevåg, *Snow Contamination of Cars: Adhesive Particle Collisions with Exterior Surfaces* (Doktorsavhandlingar vid Chalmers tekniska högskola. Ny serie).

Chalmers University of Technology, 2022, ISBN: 9789179056667. [Online]. Available: https://books.google.se/books?id=czY%5C_zwEACAAJ.

[13] M. M. M. J. Manjunatha Kannambadi. P, "Numerical simulation of water contamination around an outer rear-view mirror," Examensarbete 2022|LIU-IEI-TEK-A–22/04335–SE, 2022.

[14] J. Welty, G. Rorrer, and D. Foster, *Fundamentals of Momentum, Heat and Mass Transfer, 6th Edition International Student Version*. Wiley, 2014, ISBN: 9781118808870. [Online]. Available: https://books.google.se/books?id=oQunngEACAAJ.

[15] B. Andersson, R. Andersson, L. Håkansson, M. Mortensen, R. Sudiyo, and B. van Wachem, *Computational Fluid Dynamics for Engineers*. Cambridge University Press, 2011. DOI: 10.1017/CBO9781139093590.

[16] C. T. Crowe, J. D. Schwarzkopf, M. Sommerfeld, and Y. Tsuji, *Multiphase Flows with Droplets and Particles*, Second. Boca Raton: CRC, 2011, ISBN: 9781439840504.

[17] P. Spalart, W.-H. Jou, M. Strelets, and S. Allmaras, "Comments on the feasibility of les for wings, and on a hybrid rans/les approach," Jan. 1997.

[18] P. Spalart, S. Deck, M. Shur, K. Squires, M. Strelets, and A. Travin, "A new version of detached-eddy simulation, resistant to ambiguous grid densities," *Theoretical and Computational Fluid Dynamics*, vol. 20, pp. 181–195, Jul. 2006. DOI: 10.1007/s00162-006-0015-0.

[19] W. Hinds, *Aerosol Technology: Properties, Behavior, and Measurement of Airborne Particles*. Wiley, 1999, ISBN: 9780471194101. [Online]. Available: https://books.google.se/books?id=ORxSAAAAMAAJ.

[20] D. Guildenbecher, C. López-Rivera, and P. Sojka, "Secondary atomization," *Experiments in Fluids*, vol. 46, pp. 371–402, Mar. 2009. DOI: 10.1007/s00348-008-0593-2.

[21] P. G. Saffman, "The lift on a small sphere in a slow shear flow," *Journal of Fluid Mechanics*, vol. 22, no. 2, pp. 385–400, 1965. DOI: 10.1017/S0022112065000824.

[22] M. Sommerfeld, "Theoretical and experimental modelling of particulate flows. von karman institute for fluid dynamics 2000," 2000.

[23] P. J. O'rourke and A. A. Amsden, "The tab method for numerical calculation of spray droplet breakup," 1987.

[24] R. Reitz and R. Diwakar, "Structure of high-pressure fuel sprays," *SAE transactions*, vol. 96, pp. 492–509, 1987.

[25] J. Sternéus, T. Walker, and T. Bender, "Upgrade of the volvo cars aerodynamic wind tunnel," *SAE Transactions*, vol. 116, pp. 1089–1099, 2007, ISSN: 0096736X, 25771531. [Online]. Available: http://www.jstor.org/stable/44687874 (visited on 04/04/2023).

[26] A. B. R. Vevang, "On the prediction of exterior contamination with numerical simulations," *Fluid Dynamics Center, Volvo Car Corporation, Gothenburg, Sweden*,

A

Appendix - The Wedge

A.1 Geometry

The Wedge has previously been used for contamination testing at Volvo Cars. For instance, it was tested in a climate wind tunnel on snow experiments, which deemed it an adequate aerodynamic simplification [12]. Thus, it was an appropriate basis of design for the Wedgeoid bluff body and useful in its pre-existing absence. The Wedge is presented in Fig. A.1. The physical Wedge construction consisted of five aluminium welded surfaces with aluminium tape covering cavities. It stood on four 0.75 m long steel legs placed at the bottom exterior's center. The CAD counterpart included the main features of the real Wedge, with the exception of irregularities and roughness caused by tape, welded joints and dents in the exterior.

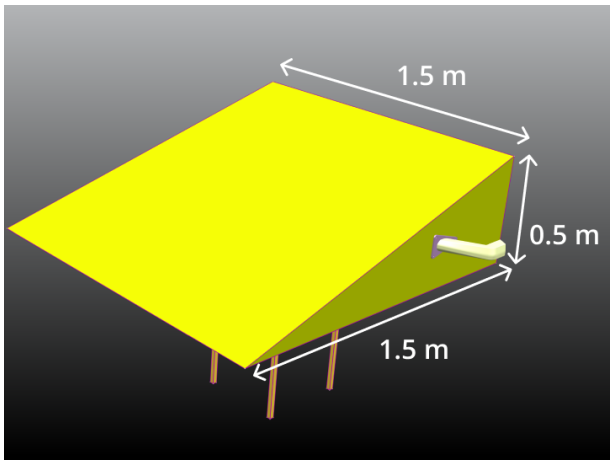

Figure A.1: *View of Wedge bluff body with attached baseline CMS in Teamcenter with dimensions.*

A.2 Experiment

The first experiment conducted at Volvo Cars' wind tunnel was conducted on the 20th of march 2023. At this point in the project, only the Baseline and Basic Groove CMS designs were available, as the remaining prototypes would be designed based in part on the results of this experiment. The primary aim was to investigate whether the baseline would get

soiled at all. It was also desired to attempt to observe droplet behaviour near and on the CMS, whether this was affected by the addition of a groove or correlated against changes in driving conditions. Finally, this experiment would provide an estimation for the upper limit of filmrupture droplet sizes.

The Wedge was used as the aerodynamic geometry, attached to the tunnel floor through its four legs set in a frame that was hinged to the floor. This setup is presented in the following Fig. A.2.

Figure A.2: *Base setup of Wedge with attached CMS in the wind tunnel.*

A.3 Results

In Fig. A.3, some observable droplet sizes from the Wedge experiment are presented. These would be used when setting the sizes of the film rupture injector. The largest droplets were assessed to be igniting from droplet migrations, but it was desired to make sure that the upper limit of rupture droplet were included, which is why it was set to 3 mm.

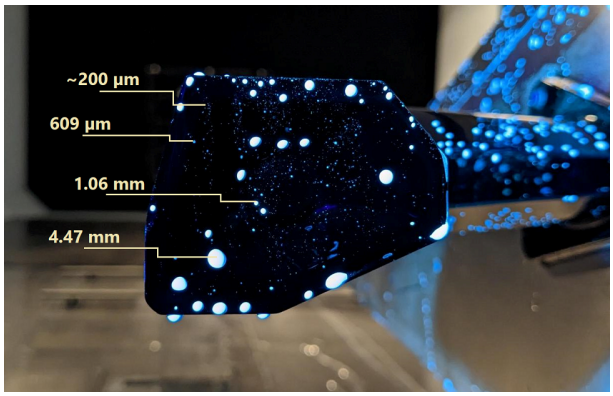

Figure A.3: *Observable droplet sizes on baseline CMS from Wedge experiment in 70 km/h.*

B

Appendix - Additional Results

B.1 Convergence of Simulations

Convergence was measured by monitoring residuals of transport entities in STAR-CCM+ which are presented in Fig. B.1 and Fig. B.2

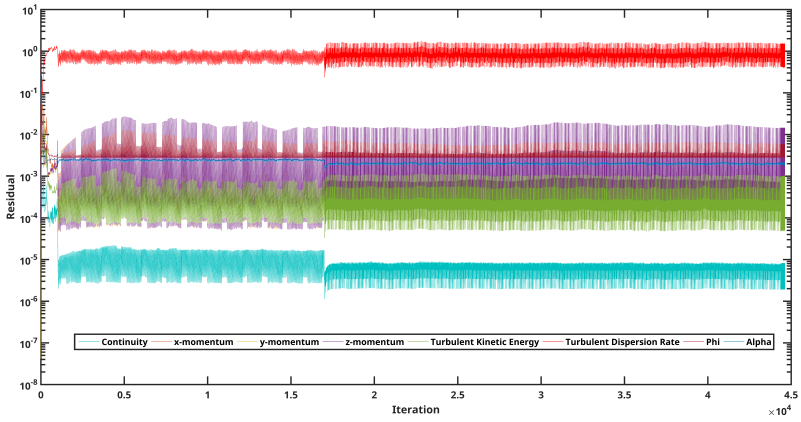

Figure B.1: *Residual plots of transport entities of simulation in Simcenter STAR-CCM+.*

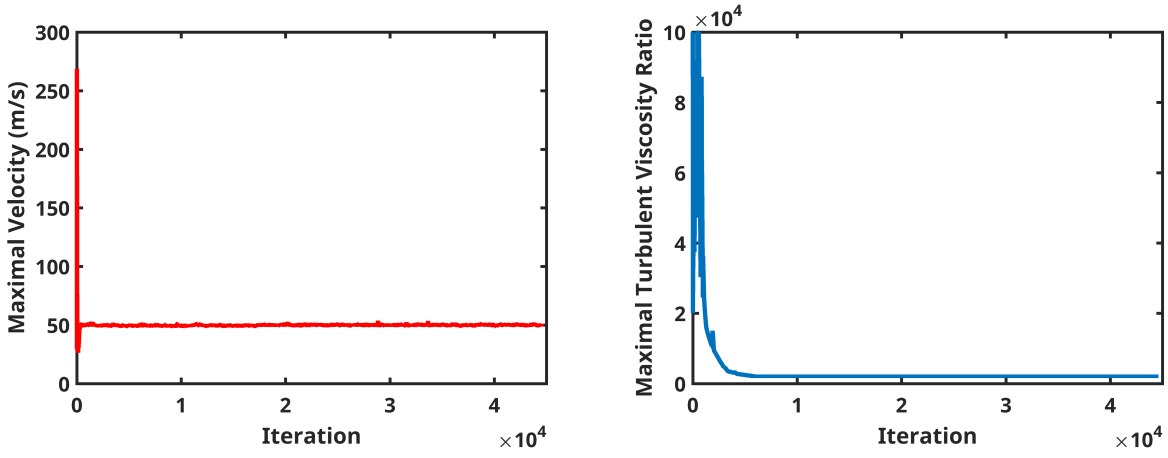

Figure B.2: *Plots of maximal velocity (L) and viscosity ratio (R) of simulation in Simcenter STAR-CCM+.*

B.2 Flow Fields

B.2.1 Baseline CMS

The mean velocity and vorticity field are presented in the Fig. B.3 and the pressure field in Fig. B.4.

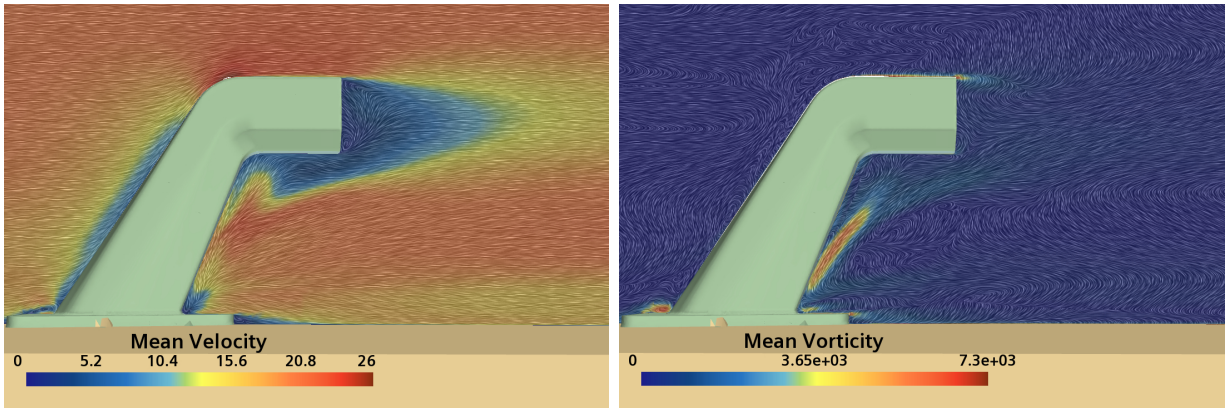

Figure B.3: *Mean velocity (L) and vorticity (R) vector fields of the CMS region.*

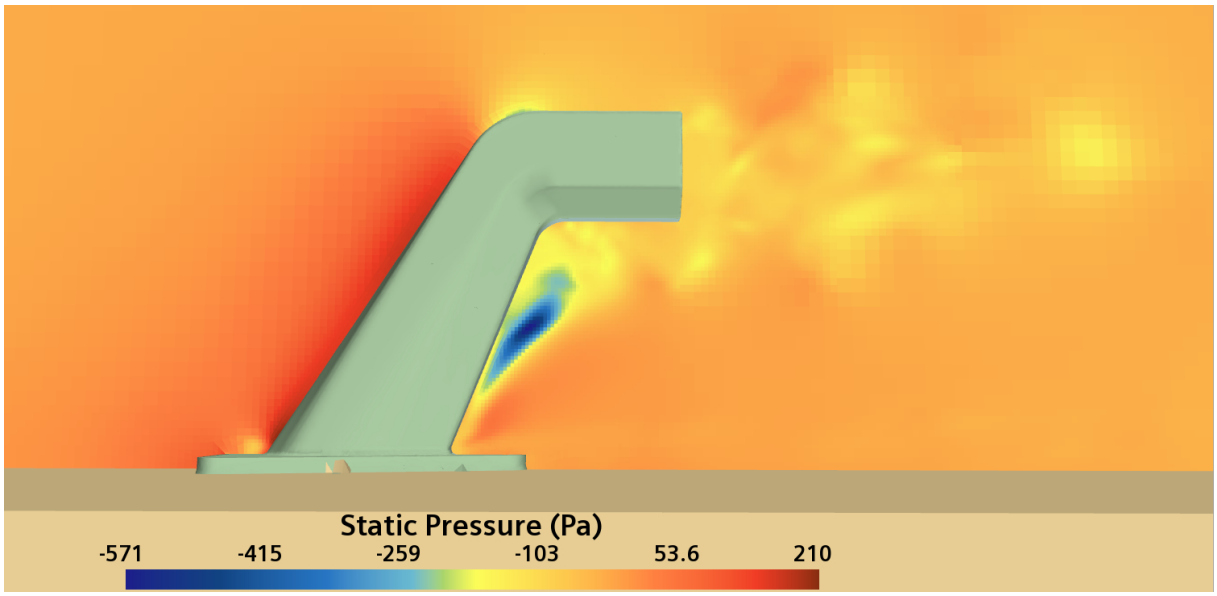

Figure B.4: *Static pressure field of CMS region.*

B.2.2 Aerodynamic Arm

The flow field of the Aerodynamic Arm design is presented in Fig. B.5.

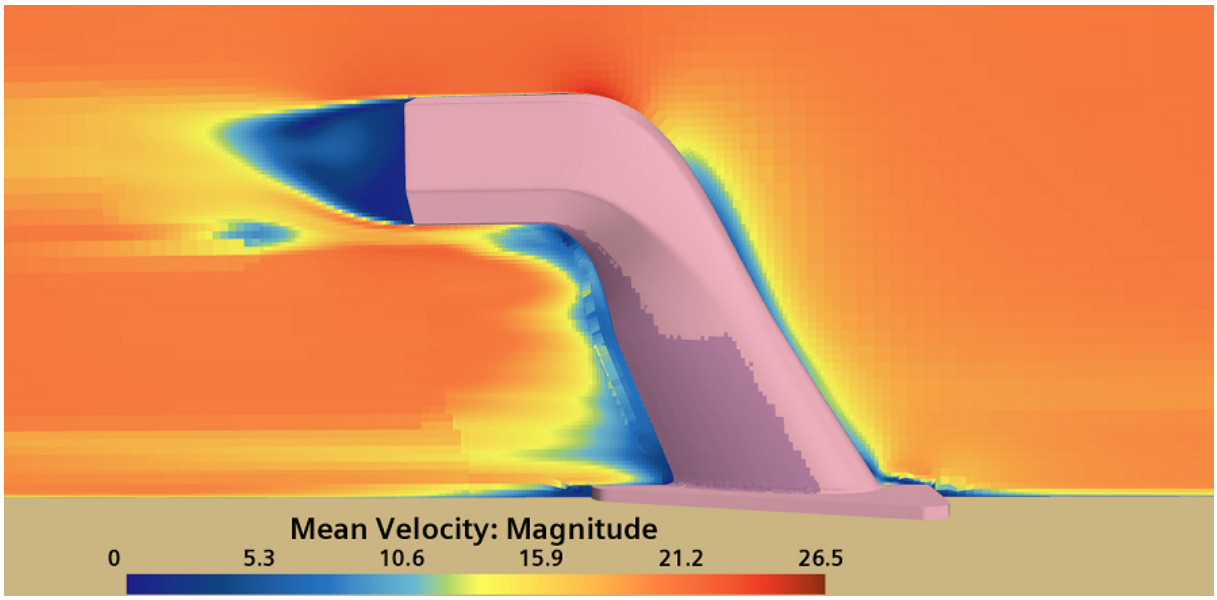

Figure B.5: *Mean velocity field of Aerodynamic Arm design in 70 km/h.*

B.3 Additional Plots

B.3.1 Baseline versus Slanted Contamination Rate

As figure 4.10 indicated that the surface coverage of the Slanted GS approached 100 %, it was of interest to examine the rate of coverage as this would indicate how rapid is soils compared to the baseline, as presented in Fig. B.6.

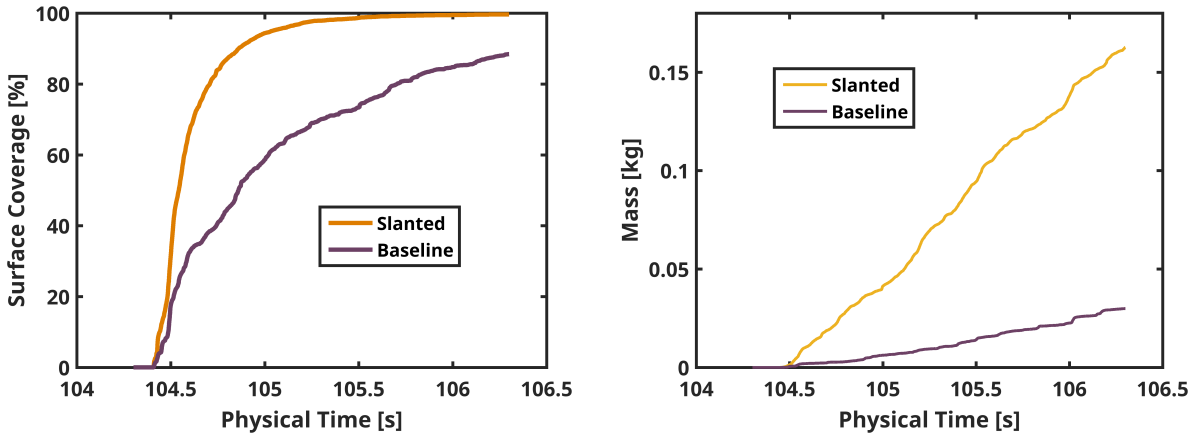

Figure B.6: *Contamination over time in simulation of baseline and Slanted GS CMS designs.*

B.3.2 Droplet Drag at Different Velocities

Since larger droplets appear to soil the baseline CMS in Fig. 4.13, it was of interest to see if this correlated with F_D. Fig. 4.4 presents the frequency distribution of F_D for the three velocities.

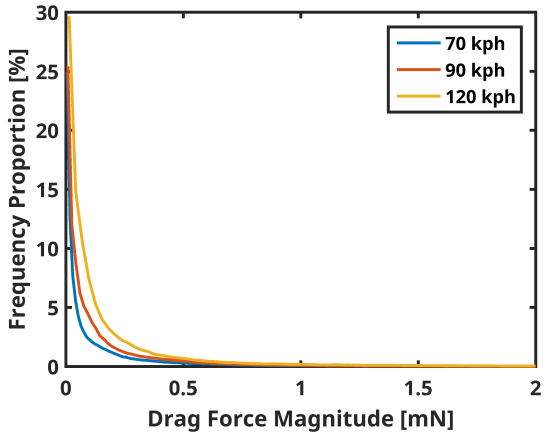

Figure B.7: *Frequency distribution of droplet drag force at 70, 90 and 120 km/h for baseline CMS simulation.*

B.3.3 Solution Sensitivity

Since the simulations are transient, the solutions aren't unique. Thus, there is an inherent difference between simulation cases, which could mean that the differences in coverage percentages could be a virtue of this difference. To account for this and estimate the transient error-marginal, Fig. B.8 presents four baseline cases

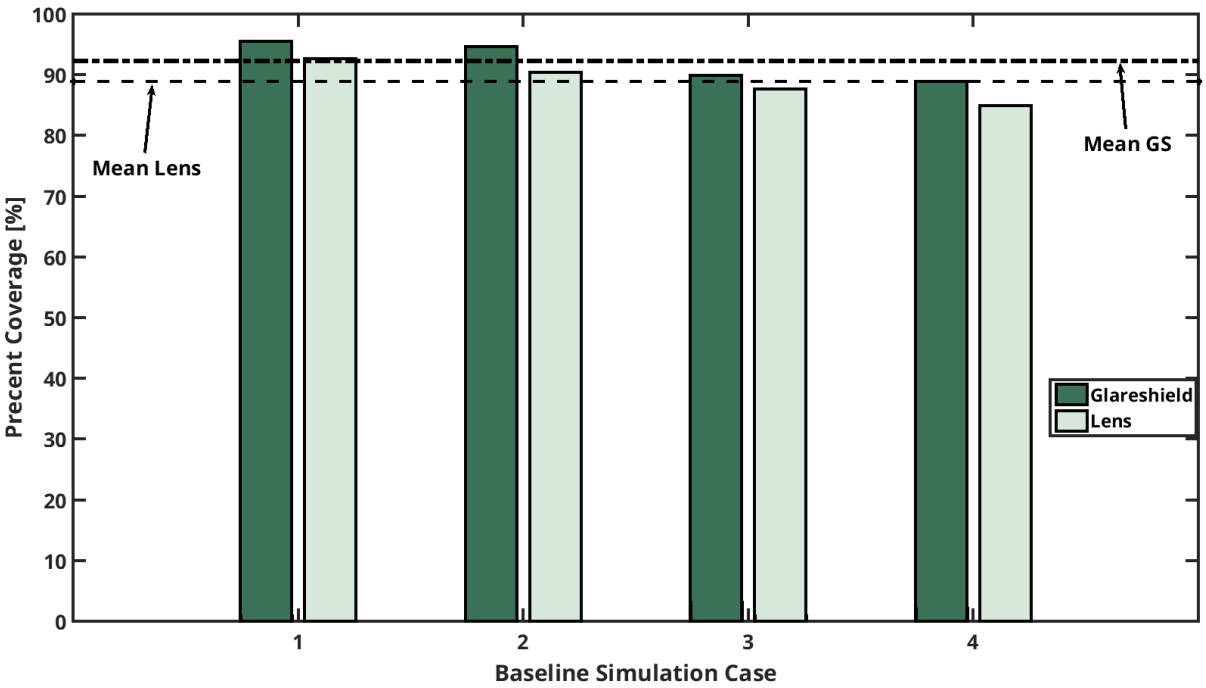

Figure B.8: *Covered CMS Glareshield and lens percentages of four baseline cases with vertical lines at the means of GS and lens.*

it may be observed that the difference is within ±3.5%-units, which means that all differences between designs observed in figure 4.10 is outside the error-marginal range.

B.4 Additional Experimental Pictures

Fig. B.9 presents a high velocity experiments were film rupture is favored over droplet migration.

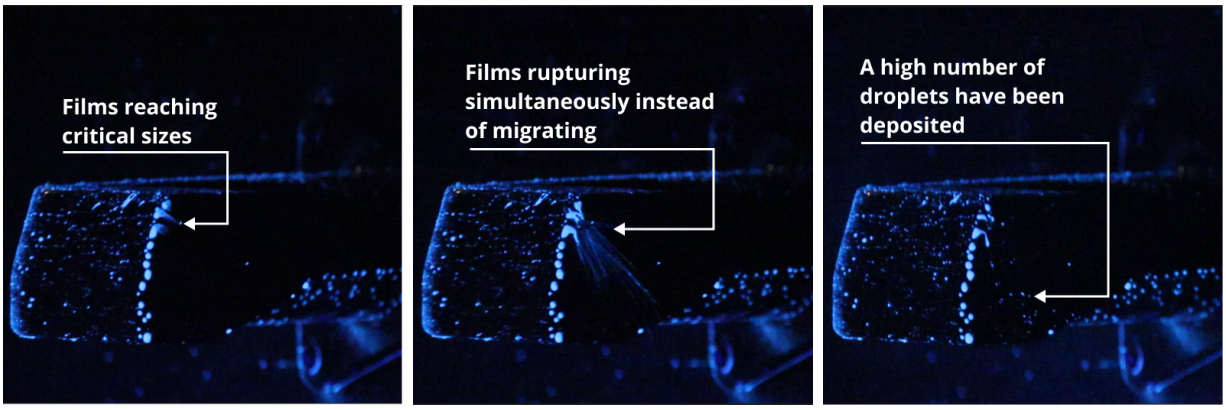

Figure B.9: *Example of when film rupture is favored over droplet migration, on baseline CMS in 120 km/h from Wedgeoid experiment.*